Journal of Dynamic Behavior of Materials
https://doi.org/10.1007/s40870-024-00413-1

RESEARCH PAPER

On the Dynamic Mechanical Behavior of Wrought and AM 17-4 Precipitation-Hardenable Stainless Steels Under Rapid Heating

S. P. Mates[1] · S. Habib[1] · J. Zuback[1] · F. Zhang[1]

Received: 19 July 2023 / Accepted: 7 February 2024

Abstract
Dynamic large-strain plasticity problems in metals can produce temperatures high enough to alter the microstructure, but the limited time-at-temperature prevents complete transformation, thereby making the material strength time-dependent. Precipitation reactions (age-hardening) are an important class of transformations that can create time-dependent dynamic plasticity under rapid heating and loading. This work explores the dynamic behavior of a precipitation-hardenable stainless steel (17-4) produced by wrought and Additive Manufacturing (AM) methods with a rapidly-heated Kolsky bar technique. Wrought 17-4, a martensitic stainless steel, is examined in three common heat treatments (solution-treated, peak-aged and over-aged) at temperatures up to 1000 °C and heating times limited to about three seconds. Solution-treated wrought 17-4 is observed to thermally-harden at aging temperatures (> 400 °C) due to rapid precipitate growth. Peak-aged precipitation strengthening becomes ineffective above 550 °C, as peak-aged material becomes indistinguishable from the solution treated-condition. Over-aged wrought 17-4 does not behave like either of the other conditions, owing to the effect of the extended heat treatment on the precipitates and on the martensite matrix. Stress-relieved AM 17-4 exhibits high dynamic strength and strain hardening at room-temperature due to its meta-stable austenite content and partial age-hardening during the build or stress-relief treatment. A plasticity model is developed for solution-treated wrought 17-4 that captures time-dependent aging effects that are derived from separate aging kinetics experiments. A separate model is developed for over-aged wrought 17-4 that contains no time-dependence as the precipitate population in this material appears to be more stable under rapid heating.

Keywords Kolsky bar · Additive manufacturing · Hybrid manufacturing · High strain rate · High heating rate

Introduction

In dynamic plasticity problems, materials often undergo very large strains in a very short time, leading to adiabatic heating sufficient to induce a microstructural transformation via processes such as grain growth, precipitation reactions or phase transformation, given sufficient time. Friction can be an important additional heat source in such problems. The rule-of-thumb microstructural stability limit at elevated temperatures is half the melting point, or a homologous temperature, T_h, below 0.5 [1]. This limit is often exceeded in problems such as machining or ballistic impact [2, 3], and some alloy systems can become unstable at lower T_h values. Further, critical temperatures are reached and/or only persist for a short time relative to the transformation time, meaning plasticity must proceed through a microstructure that differs from its quasi-equilibrium state. Unfortunately, most of our knowledge regarding the effect of temperature on plasticity is obtained from laboratory test methods that measure the quasi-equilibrium microstructural response, at least relative to dynamic timescales, and thus may not be appropriate for dynamic problems. The potential significance of this issue depends on the times and temperatures of the problem of interest and on the microstructural stability of the metal involved.

This work focuses on 17-4 precipitation-hardenable stainless steel (referred to henceforth as 17-4), a martensitic stainless steel with high strength and good corrosion resistance at elevated temperatures. Precipitation strengthening is important in many alloys and this type of transformation can create time-dependent mechanical behavior in dynamic problems,

✉ S. P. Mates
smates@nist.gov

[1] National Institute of Standards and Technology, 100 Bureau Drive, Gaithersburg, MD, USA

Published online: 06 May 2024

making this a particularly interesting alloy to examine under rapid heating and loading conditions. In the solution-treated condition (often called Condition A but henceforth called ST), 17-4 consists of un-tempered, body-centered tetragonal (BCT) martensite with a small amount of delta-ferrite [4–8]. The matrix is supersaturated with copper and contains a high density of dislocations and possibly microtwins [8]. Aging heat treatments in wrought ST temper the martensite and grow copper-rich precipitates that can increase the yield strength by hundreds of megapascals in the peak-aged condition. Precipitate growth begins near 400 °C ($T_h \approx 0.28$) [9]. Aging reactions in wrought 17-4 are well-studied, complex and produce a wide range of mechanical behavior depending on aging time and temperature [7]. At the peak aging temperature (900 °F (482 °C)), measurable strengthening occurs within seconds [10, 11] with maximum strength reached in one hour (H900 condition). Peak-aged precipitates are small (≈ 5 nm) and coherent with the martensite matrix, making them difficult to observe even in TEM. Over-aging occurs above 482 °C (900 °F) and rapidly reduces the strength as the precipitates coarsen, change shape and lose coherency with the matrix [7, 12, 13]. Over-aging at 550 °C and above for several hours heavily tempers the martensite and creates a small amount of reverted austenite, which is stable at room temperature [6] and reduces the yield strength but improves ductility [8, 9, 13]. The relative importance of tempering and austenite reversion on the mechanical behavior of over-aged 17-4 remains unclear, however [12]. Finally, peak-aged 17-4 rapidly loses strength when aged further above 550 °C [11], with prior age-hardening eliminated within seconds at 900 °C.

In addition to the aging reactions described above, the martensite-to-austenite transformation at high temperature can also cause time-dependent plasticity during fast heating. Austenite start and finish temperatures (Ac1 and Ac3, respectively) in this alloy are reported to increase with heating rate, with Ac1 ranging from 700 to 790 °C and Ac3 ranging from 880 to 930 °C [8, 11] as the heating rate increases from 1 to 1000 °C/s. During this transition, existing precipitates may either dissolve, coarsen or lose coherency with the matrix [14]. As already noted, the hardness of peak-aged 17-4 drops rapidly near Ac1 [11]. While the reported changes in mechanical behavior are ascribed mostly to evolving precipitate characteristics, direct observations of the effect of heating on precipitate populations and resulting strength levels remain elusive. Regardless of the underlying mechanisms, exploring the dynamic behavior of 17-4 under rapid heating can reveal how time and temperature affects the strength of this precipitation-hardenable stainless steel, with application to dynamic plasticity problems.

The alloy has also drawn significant attention in additive manufacturing (AM) [15–17], and the desire to improve AM part performance via hybrid manufacturing (HM) methods, including post-build surface machining, makes machinability of AM materials a growing concern. This is especially important when AM microstructures differ from wrought [18, 19]. AM 17-4 built with nitrogen-atomized feedstock powder (referred to henceforth as AM 17-4 N) contains a large amount of metastable austenite whereas wrought 17-4 is a martensitic alloy [20, 21]. Austenite in place of martensite will tend reduce the yield strength and increase the strain hardening compared to wrought 17-4 [22, 23]. Strain hardening in AM 17-4 N can also be enhanced by deformation-induced martensitic transformation (DIMT) of the austenite phase [24, 25]. Interstitial nitrogen is also known to increase the strength of austenitic and martensitic stainless steels [26–28]. High strain hardening, combined with high residual stresses in AM materials [29], can negatively affect machinability by increasing cutting forces and temperatures [30]. For this reason, and for other dynamic loading applications, the dynamic behavior of AM 17-4 N is important to explore.

While AM 17-4 N is expected to differ from wrought primarily because of its high austenite content, the dynamic behavior of wrought 17-4 is as yet not well established, with a recent exception [31]. Martensitic stainless steels generally show a positive strain rate sensitivity (increase in yield strength and decrease in strain hardening) at low temperatures [32–35]. They are also quite thermally sensitive, although dynamic strain aging can complicate their strain and strain-rate hardening and thermal softening behavior [33].

In this paper, wrought 17-4 and AM 17-4 N are examined using a rapidly-heated Kolsky bar technique with heating times limited to a few seconds prior to impact [36]. Wrought 17-4 is explored in three starting conditions: ST, peak-aged and over-aged, to examine the effects of the pre-existing precipitate population and the state of the martensite matrix on the mechanical behavior at room temperature across a range of strain rates, and in rapidly-heated dynamic tests up to about 1000 °C. AM 17-4 N is examined in the stress-relieved (SR) starting condition only. The kinetics of age-hardening in wrought ST and AM 17-4 N are measured to capture the evolution of the copper precipitate population in supersaturated material after aging at various temperatures and times. The precipitate evolution is assessed with room-temperature dynamic compression testing on the variously-aged samples. The kinetics data are then used to develop an empirical dynamic plasticity model that captures time-dependent age-hardening effects in wrought ST, including changes to dynamic strength and strain hardening, for aging times up to and including the peak-aged condition (H900). A separate model is proposed for the over-aged starting condition (H1150), which is found to behave differently than either wrought ST or H900 at high temperatures and is expected

to be more stable with respect to precipitate evolution under rapid heating compared to wrought ST.

Experimental Methods

Material Preparation and Analysis

AM 17-4 N was produced with an EOS[1] M290 400 W laser powder bed fusion machine using EOS Stainless Steel GP1 powder with a 20 µm powder layer thickness. While the powder conformed to the ASTM standard composition for 17-4 (ASTM A693-16), the build contained higher nitrogen compared to wrought, as shown in Table 1. Nitrogen content is not specified in the Standard. AM 17-4 N also contains higher carbon, nickel, copper and oxygen compared to wrought. These compositional differences may alter its mechanical behavior relative to wrought. Prior to removing the built material, the entire build plate was given a stress-relief (SR) heat treatment at 650 °C for 1 h followed by a furnace cool. Afterwards the built material was removed from the plate by Electrical Discharge Machining (EDM). Compression specimens measuring 4 mm in diameter by 2 mm thick were made from 4 mm diameter cores removed from the built material by EDM. The cores were removed parallel to, and within a few millimeters of, the build plate. Individual samples were then sliced from the cores. With reference to ISO/ASTM 52,909–2021(E), the compression axis is along the x-direction (longest dimension) and all samples have the same z-coordinate but the y-coordinate varies for different cores. All tests reported in this work involve AM 17-4 N initially in the SR condition.

Wrought 17-4 compression samples were sliced from rod stock by EDM and heat treated in vacuum at 1050 °C for 1 h followed by air cooling to room temperature to reach the solution-treated (ST) condition. Some specimens were further heat treated to the peak-aged H900 condition (480 °C (900 °F)) for 1 h followed by air cooling to room temperature and others to the over-aged H1150 condition (620 °C (1150 °F)) for 4 h followed by air cooling to room temperature.

Microstructural analysis included electron backscatter diffraction (EBSD) imaging along with energy dispersive spectroscopy (EDS) mapping. Specimens were mounted in conductive epoxy and surfaces were prepared by standard metallographic grinding and polishing steps to a 1 µm finish. Each sample was subjected to a final vibratory polishing step with 0.05 µm colloidal silica for 18 h. The EBSD and EDS data were acquired simultaneously with the sample surface tilted approximately 70° with respect to the electron beam axis using a 20 kV accelerating voltage, 4 nA beam current, 15 mm working distance, and a 0.25 µm step size. Solutions for each Kikuchi pattern were confined to ferrite/martensite, austenite, or Nb(C, N), and no distinction was made between ferrite and martensite due to the low tetragonality of the martensite unit cell. Inverse pole figures (IPF) and phase maps were constructed by removing zero solutions to individual EBSD patterns for visual purposes. Boundaries representing an arbitrary 10° misorientation angle in the data were applied to each image for contrast. Complementary phase fraction and lattice parameter measurements were performed on all four materials using high-energy X-ray diffraction (HEXRD) at beamline 1-ID of the Advanced Photon source. The X-ray energy was 61.33 keV (wavelength: 0.2022 Å). We collected the data in the transmission mode with an approximate sample thickness of 1 mm. We used a Varex 4343CT amorphous silicon area detector for data collection. More details of this setup can be found elsewhere [37].

Servohydraulic Mechanical Testing

Quasi-static compression experiments were conducted using a servo-hydraulic testing machine at nominal strain rates of 0.0003 1/s and 0.03 1/s outfitted with a 50 kN load cell. A custom compression fixture was developed to limit buckling at larger strains that employed tungsten carbide platens and high vacuum grease lubricant. Stereo digital image correlation (DIC) was used to measure the surface strains and monitor buckling and barreling during testing. DIC measurements were performed using two 12 megapixel cameras and macro lenses that yielded an imaging resolution of 6.1 µm/

Table 1 Chemical composition of wrought and AM samples in mass fraction (%), with the balance being Fe

Element	Cr	Ni	Cu	Nb	Mn	Mo	C	N	O	P	Si	S
Wrought[a]	15.1	4.07	3.66	0.26	0.93	0.21	0.03	0.044	0.004	0.025	0.4	0.025
AM[a]	15.3	4.4	4.41	0.28	0.72	0.11	0.05	0.12	0.031	0.004	0.58	0.004
Standard Specification[b]	15.0 to 17.5	3.0 to 5.0	3.0 to 5.0	0.15 to 0.45	1.00	n/a	0.07	n/a	n/a	0.04	1.0	0.03

[a]ASTM E1019/E415. The measurement uncertainty is ±5% of the value for elements between 5% and 24.99%, ± 10% of the value for elements between 0.05% and 4.99% and ±25% of the value elements less than 0.05%

[b]ASTM A693-16. Single values indicate the maximum amount permitted by the standard

pixel. Correlated Solutions Vic3D[1] was used for the DIC calculations with a subset size, step size, and filter size of 29 pixels, 10 pixels, and 5 pixels, respectively, resulting in a virtual strain gauge size of 0.42 mm and an average spatial standard deviation of 257 μm/m [38]. The cylindrical quasi static compression specimens were machined with a length of 7.14 mm and a diameter of 4.76 mm for all wrought conditions, and a length of 6 mm and a diameter of 4 mm for AM 17-4 N to achieve a length to diameter ratio of 1.5. A virtual DIC strain gauge of 6 mm and 4 mm was used to represent the strains for the wrought conditions and AM 17-4 N, respectively.

Pulse-Heated Kolsky Bar Technique

The mechanical arrangement for the pulse-heated Kolsky bar [36] consists of twin (1.5 m by 15 mm diameter) maraging steel bars in the un-hardened condition, with a Young's modulus and wave speed of 170 GPa ± 2 GPa and 4600 m/s ± 25 m/s, respectively. Short (3 cm) sections of hardened maraging steel were threaded into the main bars at the impact ends for added strength and to facilitate repairs from heat or electrical arcing damage after many heated tests. All tests employed a 375 mm long striker bar with impact velocities ranging from 9.5 to 13.5 m/s ± 0.2 m/s.

Samples were electrically heated with direct electric current flow through the bar tips and sample. Graphite foils were placed between the sample and the bars to eliminate electrical arcing that would otherwise spot-weld the sample to the bars. The foils also provided some lubrication during compression testing. Elastic bands were used to slightly pre-compress the sample and foils to improve the electrical and thermal contact with the bars. A vacuum chamber was placed around the sample and bar ends to reduce sample oxidation during heating. The vacuum also provided some additional pre-compression on the sample and foils. The overall pre-compression force was negligible compared to the testing forces. Heating currents were generated by a low-voltage battery bank (13.2 V) to achieve transient heating rates up to 1000 °C/s and to maintain steady temperatures for several seconds. Precise control of the shape and duration of the sample temperature history was achieved with feedback control on either the heating current level or the sample surface temperature. For controlled-temperature experiments, the surface radiance temperature was measured with a high-speed (800 kHz bandwidth) wide-band near-infrared pyrometer with a 1.2 μm central wavelength and a spot size of 1 mm^2. Current-controlled experiments, used for low temperature tests where the thermal radiance signal is below the noise floor of the pyrometer, relied on the voltage drop across a precision resistor. The heating current was extinguished about 20 ms prior to the arrival of the elastic loading wave to avoid arcing as the bars became separated after impact.

For the stress-strain analysis, the incident and transmitted strain wave pulses, measured at 2 MHz, were analyzed using the basic methods described in a number of articles [39–41], but with three noteworthy exceptions. First, analysis of the heated experiments considered the deformation behavior of the graphite foil separately from the sample [36]. The next two exceptions applied to all tests. An elastic "punching" correction [42] was applied to account for elastic indentation of the bar contact faces, and a two-wave stress-strain analysis technique was employed to avoid errors associated with the delayed recovery of the gage strain from prior wave passages which biased the reflected wave signal. In this technique, the reflected pulse was computed from the difference between the incident and transmitted pulses. All tests were pulse-shaped with annealed copper disks (6.35 mm diameter and 0.254 mm thick) to smooth the stress-strain results. Uncertainties in the stress-strain measurements were estimated from random error propagation and considering uncertainties in the gage strain, the bar material properties, the specimen dimensions, and the foil deformation for heated tests. The foil deformation uncertainty dominated the overall stress-strain uncertainty for heated tests. Two additional room temperature Kolsky bar tests were performed at intermediate strain rates (approximately 790 1/s to 1000 1/s) to better establish the strain rate sensitivity of the ST condition. These tests used thicker samples (length/diameter = 1.0), and while these experiments were used for model fitting, they were not shown in every figure.

For the thermal analysis, true temperatures were measured with a Type K thermocouple (0.127 mm diameter wire) spot-welded to the sample surface away from the pyrometer spot, with a distributed junction and a physical ice point reference. Locating the thermocouple away from the pyrometer spot avoided blocking the radiance signal and aided the detection of poor heating uniformity, as described below. During heating, the thermocouple signal was heavily biased by the electromagnetic field associated with the heating current. The bias decayed within a few milliseconds after current shut-off, allowing reliable temperature measurements just before the sample was dynamically loaded. The thermal history was then deduced from the pyrometer radiance temperature and an effective surface emissivity determined from the thermocouple reading prior to impact.

Thermal and mechanical data acquired during a typical heated compression experiment are shown in Fig. 1. The

[1] Certain equipment, instruments, software, or materials are identified in this paper in order to specify the experimental procedure adequately. Such identification is not intended to imply recommendation or endorsement of any product or service by NIST, nor is it intended to imply that the materials or equipment identified are necessarily the best available for the purpose.

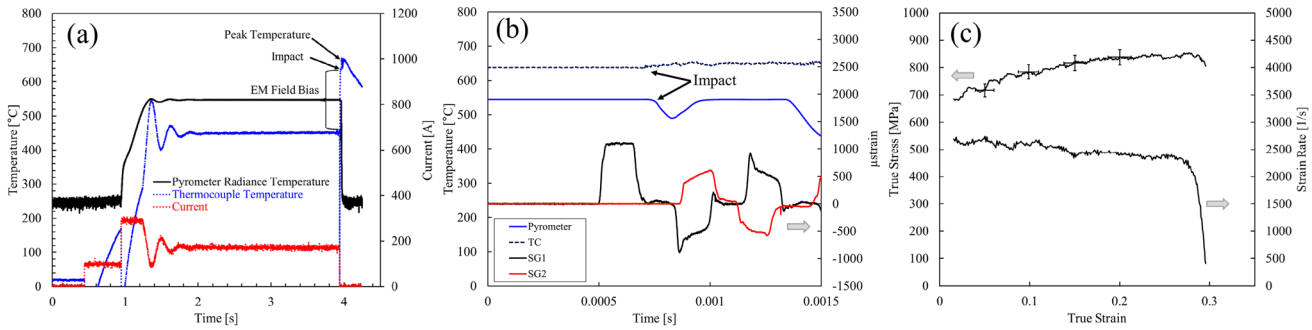

Fig. 1 Typical heating experiment showing thermal history (**a**), thermal and strain gage signals at impact (**b**) and true stress versus true strain and true strain rate versus true strain data (**c**) for an experiment with an impact temperature of 626 °C ± 40 °C

total heating time was 3.5 s. The first 0.5 s consisted of a 75 A pre-heat cycle that established a steady current flow path and eliminated arcing that would occur has the maximum test current been applied immediately. The sample was then brought to a steady temperature within about the next 0.9 s, with some underdamped oscillations noticeable in the heating current. This was followed by a constant temperature hold period until impact. The hold period promoted good temperature uniformity and test repeatability over a wide temperature range while maintaining a short overall heating time. Faster heating rates (e.g. shorter hold times or ramp tests) can also be achieved with this technique. The thermal history plot (Fig. 1a) demonstrates the EM field bias picked up by the thermocouple and how it disappears quickly after the heating circuit is broken allowing an accurate thermocouple reading at the moment of impact, shown in Fig. 1b. Figure 1a also notes how the peak thermocouple temperature is well above the impact temperature due to the adiabatic temperature rise resulting from plastic deformation. The time period shown in Fig. 1b is too constrained to show the peak temperature achieved by the thermocouple. Also, although the pyrometer signal appears to recover after impact, post-impact data is unreliable because the sample moves out of the pyrometer's field of view, making it unclear what the pyrometer is viewing. The dynamic stress-strain and strain-rate-strain results are shown in Fig. 1c, corrected for graphite foil deformation and with uncertainty estimates for several points along the stress-strain curve.

The temperature measurement uncertainty estimate accounted for two primary sources, one being the uncertainty of the surface temperature measurement, and the other being the internal temperature gradient within the sample due to heat conducted into the much cooler Kolsky bars. The thermocouple signal has a low inherent uncertainty (the greater of ± 2.2 °C or ± 0.75% [43]) provided the spot weld is good. Poor welds were diagnosed by an unrealistically large difference between the thermocouple and pyrometer signals. The surface temperature uniformity degrades due to poor thermal/electrical contact between the sample and bars, although good installation methods and precompression loading mitigate this problem. Good surface temperature uniformity is indicated by a close and predictable relationship between the thermocouple and radiance temperature signals, which is quite linear. As the thermocouple and pyrometer view different locations on the sample, the uncertainty related to surface temperature uniformity can be estimated from the difference between a given pyrometer temperature measurement and the value predicted from the linear relationship established for the overall dataset. Experiments having large deviations, or those where the thermocouple reading was equal to or less than the pyrometer radiance temperature, indicating poor thermocouple attachment, were rejected. The effective sample temperature is then computed by accounting for the internal temperature variation in the sample, which is estimated using finite element analysis [44]. The sample temperature peaks in the center and decreases toward the bar interfaces as the sample cools sightly just prior to impact. Hence, the effective sample temperature at impact, T_{test}, equals the thermocouple temperature, measured near the middle of the sample, minus half the axial temperature gradient, shown in Eq. 1 below. The uncertainty is computed from the thermocouple temperature, T_{TC}, the measured pyrometer radiance temperature, $T_{\text{pyro,measured}}$, the pyrometer temperature predicted from T_{TC} ($T_{\text{pyro,predicted}} = 0.94\ T_{\text{TC}} - 37.4$), and the estimated temperature variation inside the sample, $\Delta T_{\text{variation}}$, as follows:

$$T_{\text{test}} = \left(T_{\text{TC}} - \frac{\Delta T_{\text{variation}}}{2}\right) \pm \left(\Delta T_{\text{pyro}} + \frac{\Delta T_{\text{variation}}}{2}\right) \quad (1)$$

$$\Delta T_{\text{variation}} = 0.0456 * T_{\text{TC}} - 0.0367 \quad (2)$$

$$\Delta T_{\text{pyro}} = Avg\left[abs\left(T_{\text{pyro,measured}} - T_{\text{pyro,predicted}}\right)\right] \quad (3)$$

The adiabatic temperature rise resulting from dynamic compression is calculated as a function of plastic strain using Eq. 4 below, which employs a temperature-dependent heat capacity given by $c_p = 247.03 + 0.9632T$ J/(kg K) [32]:

$$T_{\text{adiabatic}} = T_{\text{initial}} + \frac{\eta \int_0^{\varepsilon} \sigma d\varepsilon}{\rho\left(247.03 + 0.9632\, T_{\text{adiabatic}}\right)} \quad (4)$$

Here ρ is the density (7 780 kg/m^3) which is considered constant, σ and ε are true stress and true strain, and η is the Taylor-Quinney coefficient, assumed to be 0.9. Equation 4 is solved iteratively at each strain value considering the adiabatic temperature increase at each strain step using the measured initial temperature, T_{initial}. Estimating adiabatic temperatures for each strain value in dynamic test results is necessary to develop appropriate fits to the kinetic and plasticity models that are described later. The temperature rise associated during the plastic deformation process cannot be measured directly with the thermocouple due response time limitations. Adiabatic temperatures are not estimated for the quasi-static tests.

Aging Kinetics Experiments

Aging experiments on wrought ST and AM 17-4 N were performed to establish time- and temperature-dependent aging kinetics relevant to their possible time-dependent dynamic mechanical behavior. As noted, partial aging of the AM 17-4 N probably occurred during the build or stress-relief heat treatment (evidence is given later in the paper), but its subsequent aging potential was also of interest to explore. Wrought ST samples were aged near the peak aging temperature (500 °C ± 10 °C) between 0.2 and 3600 s, and two over-aging temperatures (564 °C ± 10 and 663 °C ± 9 °C) between 0.2 and 1000 s. Aging treatments were performed using a combination of electrical heating, a salt bath and a conventional furnace. Samples heated electrically were then rapidly cooled from the aging temperature by heat conduction into the Kolsky bars (peak cooling rate of about 500 °C/s) while those aged in the salt bath and the furnace were air cooled (peak cooling rate of about 50 °C/s) to room temperature. Aging tests on AM 17-4 N were performed at 500 °C ± 10 °C for various aging times up to 3600 s. Aged specimens were tested at room-temperature Kolsky bar experiments to determine the effect of aging on the dynamic stress-strain behavior.

Results and Discussion

Microstructural Analysis

Figure 2 reveals the microstructures of the four materials investigated via IPFs obtained for the normal direction of the sample surface (IPF-Z) along with corresponding phase and EDS maps which identify the crystallographic phases present and niobium rich precipitates, respectively. The IPF-Z and phase maps are overlayed on band contrast maps for improved visualization of the microstructural features. All three wrought materials display an equiaxed martensitic grain structure of similar scale, confirming that neither the H900 nor H1150 heat treatments significantly change the austenite grain size from the solution-treated condition. The martensite packet sizes, revealed by misoriented bands within prior austenite grains, are also qualitatively similar among the three wrought materials. Many of the lath blocks are separated by high angle grain boundaries. The phase maps show a significant amount of reverted austenite in H1150 with less observed in H900. Maps acquired at higher magnifications indicate the austenite amounts to about 5% by volume in the H1150 sample compared to approximately 1% in H900. Austenite in H1150 appears mostly along prior austenite grain boundaries, in blocky form, and within martensite grains, typically as thin, inter-lath layers. Niobium-rich precipitates are revealed by EDS measurements in all wrought samples. They are assumed to be Nb(C,N), as Nb is added to consume carbon and nitrogen, and in so doing to prevent the growth of chromium carbides that can degrade corrosion resistance by depleting Cr from the matrix [4]. Nb(C,N) precipitates do not affect strength or ductility but their presence lowers the amount of interstitial carbon and nitrogen in the matrix which can reduce its strength [45, 46]. Copper precipitates in H900 and H1150 are below the resolution of both the EBSD and EDS measurements.

The AM 17-4 N microstructure displays features indicative of the AM build process: grain boundaries are often curved and grains are elongated rather than equiaxed. We note that the surface revealed in EBSD image has likely undergone transformation to martensite (DIMT) during the metallographic preparation [47] which reduces the amount of austenite indicated (≈5 %) compared to expectations [16]. This also may affect the apparent grain size indicated by the EBSD image, so no grain size analysis was attempted. AM 17-4 N has no Nb(C,N) precipitates unlike wrought 17-4. Nb(C,N) precipitates form during solution heat treatment in wrought processing (1 h at 1050 °C), conditions that do not occur during the AM build process or the stress-relief heat treatment. The absence of Nb(C,N) implies higher levels of C and N may be present in solid solution in AM 17-4 N, which may tend to increase the martensite strength [45] and the stability of the retained austenite [4].

Austenite phase fraction and lattice parameter measurements obtained by HEXRD are shown in Fig. 3, and the phase fractions are compared with EBSD results in Table 2. Based on repeated measurements with different magnifications (pixel size vs. feature size), the estimated bias in austenite fraction measurements from EBSD is about 1%. However other sources of bias are possible. Austenite phase fractions are systematically larger when measured by HEXRD. Wrought ST and H900 have very

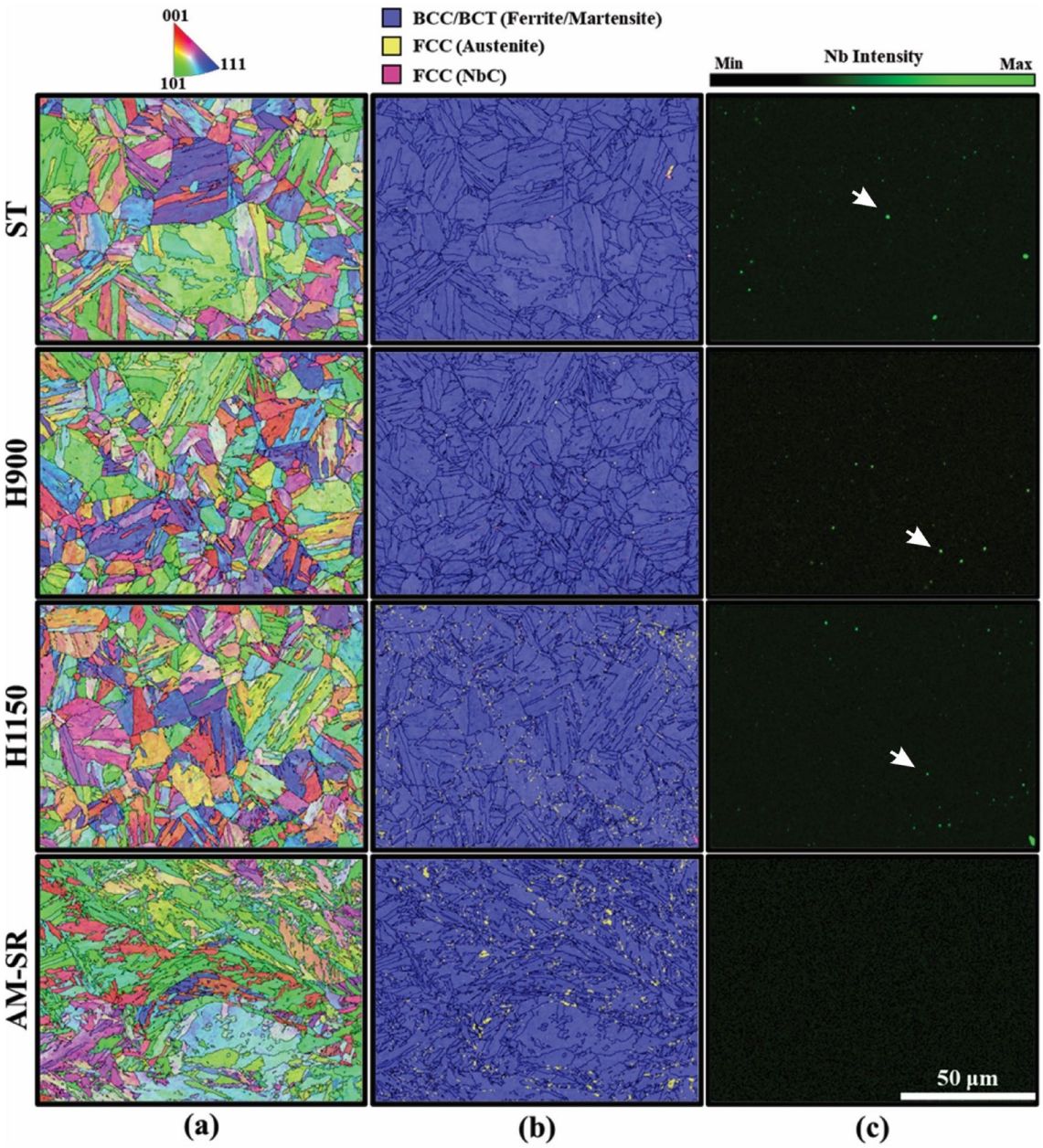

Fig. 2 Microstructural images of (**a**) IPF-Z, (**b**) phase maps, and (**c**) EDS maps of Nb for the wrought ST, wrought H900, wrought H1150, and AM 17-4 N. The IPF-Z and phase maps are overlayed on band contrast images to highlight microstructural features. Arrows on EDS maps indicate evidence of Nb(C,N).

small austenite fractions, while H1150 has almost 10% by volume according to HEXRD but only 5% according to the EBSD measurements. AM 17-4 N shows the largest discrepancy, with EBSD indicating about the same as that found in wrought H1150 while HEXRD indicates almost 30% austenite by volume. Metastable austenite in AM 17-4 N has been shown to transform during mechanical polishing, causing EBSD methods to report artificially low austenite volume fractions [47]. It is unclear if the same issue explains the different austenite fraction measurements for the wrought H1150. Another possible cause for the discrepancy in the H1150 austenite fractions is that some of the inter-lath austenite formed during over-aging may be too small to be resolved in the EBSD maps.

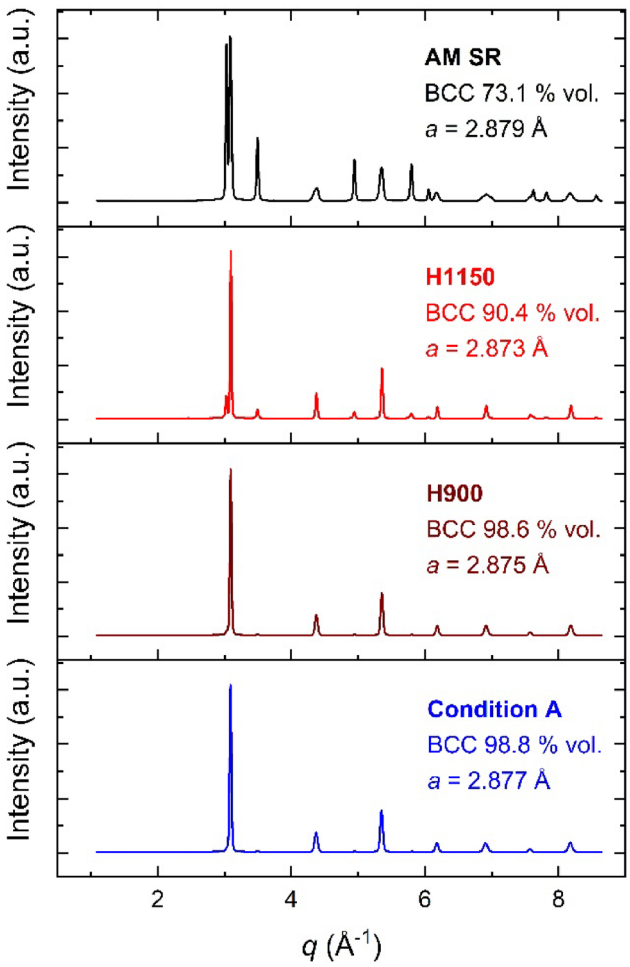

Fig. 3 Volume fractions of BCC phase and BCC lattice parameter measurements of wrought 17-4 in the solution treated (ST) condition (Condition A) and the H900 and H1150 heat treatments along with AM 17-4 N determined by HEXRD. The balance phase is FCC.

Room Temperature Mechanical Behavior at Different Strain Rates

Figure 4 shows room temperature stress-strain curves of wrought 17-4 in the ST, H900 and H1150 conditions along with AM 17-4 N at different strain rates obtained from servo-hydraulic and Kolsky bar tests. Because the Kolsky bar data are uncertain near the yield point due to the rapidly changing strain rate in this portion of the test, stress-strain data were plotted only at strains where the strain rate has stabilized. All three wrought alloys showed a similar, positive strain rate sensitivity. H900 was stronger and exhibited higher strain hardening compared to solution-treated material at all strain rates. Peak aging increased the dynamic flow stress by about 400 MPa at 0.075 strain (comparing H900 to ST), and similar strengthening was observed at quasi-static strain rates. Strength comparisons were made at 0.075 plastic strain out of convenience as this strain level is attained in all experiments and the strain rate was always stable. The strength of ST and H1150 increased by approximately 16% between the lowest and highest strain rates examined, while H900 increased by only 9%, when observed at 0.075 strain. Reduced strain-rate hardening in H900 may be due to the lower peak strain rate attained in the Kolsky bar tests. As such, the peak-aging heat treatment appears to have only a small effect on strain rate sensitivity, although further experiments are needed to draw firmer conclusions.

The high strain hardening observed in H900 has also been reported at quasi-static strain rates [5, 48]. One source could be martensite tempering resulting from the H900 heat treatment. Recovery of the martensite matrix has been observed by TEM [6]. Austenite reversion may contribute, but both HEXRD and EBSD results show H900 has very little austenite. In addition to the effects due to austenite, precipitates can also increase strain hardening, but they are usually associated with the Orowan looping rather than particle splitting [49]. Splitting is more likely for the precipitates in H900, which are nanometer-scale. Orowan looping is more likely to occur with the over-aged precipitates in H1150, and indeed the strain hardening is elevated compared to ST but still low relative to H900.

AM 17-4 N showed higher strength compared to wrought ST and, after possible extended yield point behavior [23], it strain-hardens more than wrought ST at all strain rates. AM 17-4 N also shows more complex rate-sensitivity compared to wrought due to its high metastable austenite content. Austenitic stainless steels can exhibit high strain hardening due to DIMT or twinning, depending on temperature and strain rate [50]. Increasing strain rates lead to higher

Table 2 Comparison of BCC and FCC volume fractions from EBSD and HEXRD.

Material	EBSD BCC (Vol %)	EBSD FCC (Vol %)	EBSD Zero solutions (Vol %)	HEXRD BCC (Vol %)	HEXRD FCC (Vol %)
Condition A	98.6	0.1	1.22	98.8	1.2
H900	97.3	0.80	0.86	98.6	1.4
H1150	92.7	4.5	2.63	90.4	9.6
AM 17-4 N	92.7	5.0	2.28	73.1	26.9

Remainder of EBSD phase volume fractions are Nb(C,N)

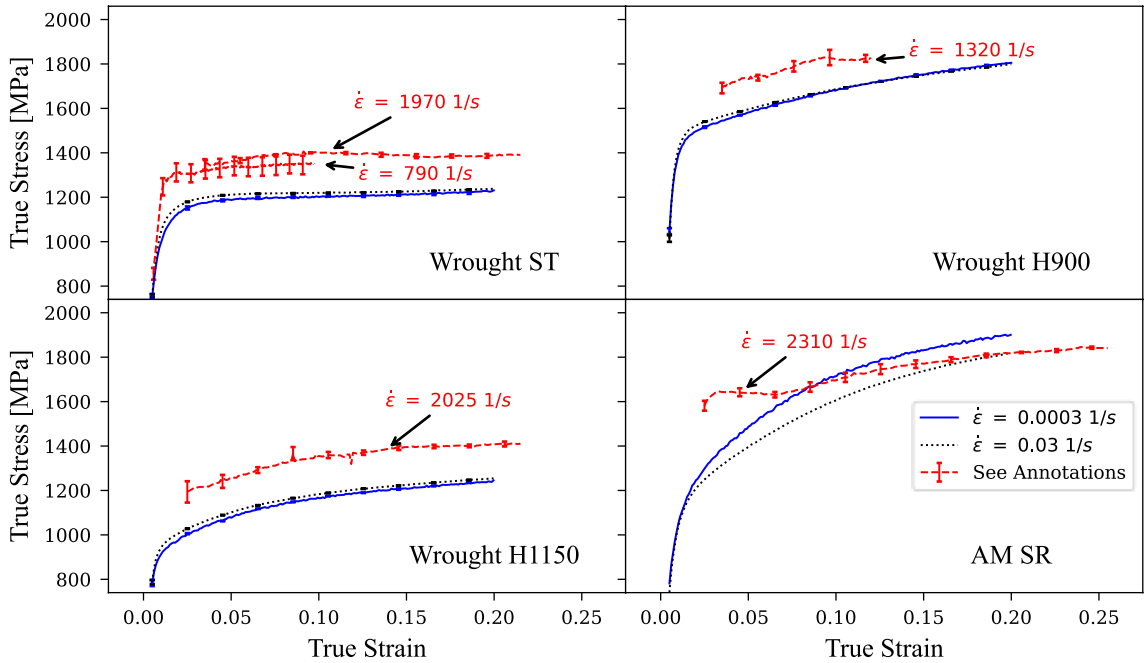

Fig. 4 Room temperature compressive stress-strain behavior of wrought 17-4 ST, H900 and H1150 along with AM 17-4 N at three strain rates. Error bars on the Kolsky bar data represent one standard deviation of the mean of 5 replicates. Quasi-static data are the average of two replicates, with negligible deviation

yield stresses and reduced strain hardening in fully austenitic stainless steels, and this has been attributed to adiabatic heating reducing the driving force for DIMT [51]. The high yield strength of AM 17-4 N relative to wrought is unexpected, given that austenite is usually weaker than martensite given similar compositions. As noted earlier, age hardening may occur in AM 17-4 N during either the build process or the stress relief heat treatment. This is explored later in this paper. Regardless of the causes, the relatively high strength and high strain hardening will make AM 17-4 N significantly more difficult to machine compared to wrought ST [3].

Dynamic Behavior at Elevated Temperatures

Figure 5 shows the effect of temperature on the dynamic flow stress and strain hardening behavior of wrought 17-4 in the solution-treated (ST), peak-aged (H900), and overaged (H1150) conditions, along with AM 17-4 N in the stress-relieved condition. Representative error bars on temperature and flow stress are provided for a few data points with the rest omitted for clarity. The average strain rate in the experiments increased from about 1300 1/s at room temperature to about 4500 1/s at the highest temperatures due to the decreasing flow stress of the samples and the use similar striker velocities for all tests. Increasing strain rates will have a small influence on the apparent temperature sensitivity in the raw data, but these effects are fully accounted for when fitting the temperature sensitivity parameters, as will be discussed later. The flow stress data are plotted versus adiabatic temperature (Eq. 4) to facilitate comparisons with the model fit results presented later. In discussing the elevated-temperature results, it is convenient to define the different temperature ranges corresponding to the different categories of precipitation reactions or phase transformations expected, as they each have distinct influences on mechanical behavior. Low temperature (< 450 °C) describes the range where no precipitation reactions are expected, peak aging (450 to 550 °C) describes the range where peak age hardening occurs after 1 h and where over-aging is limited, over-aging (550 to 750 °C) describes where both age-hardening and age-softening (over-aging) are possible depending on the starting condition (aged or not) and heating times, and austenite range (> 750 °C, nominally the middle of the Ac1 temperatures reported in the literature) describes where the crystal structure is transitioning to, or has transitioned to, austenite. These definitions are approximate only, based on the dataset at hand along with our interpretation of the literature, and should therefore be regarded as qualitative. Further, while these boundaries ignore kinetics, the described reactions are likely to occur within the timescales of interest in this work (seconds to hours). The temperature boundaries are plotted as vertical lines in Fig. 5 as a visual aid.

Beginning with the low temperature region, all three wrought materials showed significant thermal softening. Age hardening effects, marked by the strength difference between ST and H900, decreased steadily from room temperature,

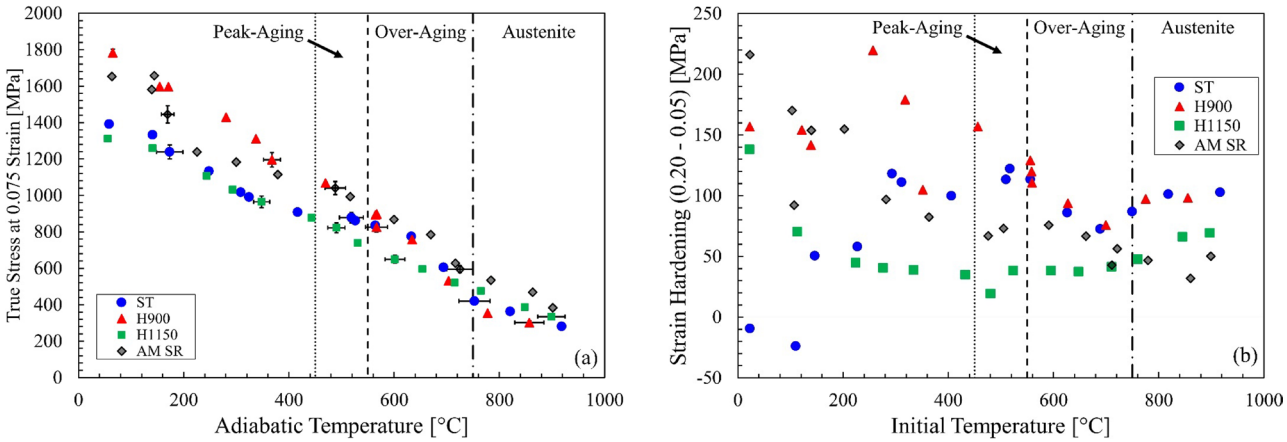

Fig. 5 Elevated-temperature dynamic flow stress data at a plastic strain of 0.075 (**a**) and strain hardening data between plastic strains of 0.05 and 0.20 (**b**) for wrought ST, H900 and H1150 an AM 17-4 N with uniform heating times of 3.5 s. Error bars (k = 2) were computed as described in Experimental Methods and are similar for all data points in both plots. The average strain rate in the experiments ranged from 1300 to 4500 1/s

becoming essentially imperceptible in the over-aging temperature range and beyond. ST strengthened with temperature near the peak aging range, while H900 continued to soften through this range, bringing the two data sets into accord with one another above about 600 °C. Near the beginning of the austenite range, both ST and H900 experienced accelerated thermal softening and upturns in strain hardening, both effects in keeping with a martensite-to-austenite transition. H900 showed the highest strain hardening among the wrought materials from room temperature up to the over-aging range. ST displayed virtually no strain hardening at room temperature but its strain hardening increased rapidly with temperature, eventually matching H900 in the over-aging range and above. Wrought ST also showed slightly higher strain hardening levels in the peak aging region. Both ST and H900 showed identical increases in strain hardening with temperature in the austenite region.

H1150, with a population of large, over-aged precipitates that are relatively stable for short heating times, had a similar flow stress compared to ST at low temperatures and at 0.075 strain, but it showed different strain-hardening behavior. At peak aging temperatures and above, however, H1150 deviated significantly from ST and H900. It thermally softened with a nearly constant slope over the entire temperature range, displaying neither the strengthening observed in ST at aging temperatures nor the accelerated softening near the austenite transition observed in both ST and H900. In the austenite range, H1150 was mildly stronger than the other two at 0.075 strain, and the upturn in strain hardening that occurs near the beginning of the austenite range was less pronounced.

As at room temperature, the mechanical behavior of AM 17-4 N in elevated-temperature dynamic tests was different from the wrought materials. AM 17-4 N showed a strength level in between wrought ST and H900 at low temperatures, but higher strengths at aging temperatures and higher, extending into the austenite range. Its flow stress was nearly temperature-insensitive up to about 150 °C, after which it dropped rapidly before resuming a steadier thermal softening behavior with further temperature increases. AM 17-4 N displayed the highest strain hardening from room temperature up to 150 °C, after which both its strength and strain hardening fell to a lower trendline. That AM 17-4 N showed a substantial decrease in both strength and strain hardening at above 150 °C in dynamic tests may represent a transition from DIMT or twinning-dominated deformation at low temperatures to thermally-activated slip dominated deformation at higher temperatures, where the DIMT driving force is reduced. The mild upturn in strain hardening observed in AM 17-4 N at aging temperatures may be due to rapid age hardening, as with wrought ST. Finally, in the austenite region, the upturn in strain hardening associated with the austenite-to-martensite transformation was delayed to higher temperatures compared to wrought, although the data are scarce and therefore not conclusive.

Discussion of Experimental Results

The strength plateau observed in wrought ST at aging temperatures is assumed to be due to rapid age-hardening. A different aging effect, dynamic strain aging (DSA), can produce similar strength plateaus and higher strain hardening values in elevated-temperature dynamic tests like these, especially in plain carbon steels [44]. However, H900 showed no strength or strain hardening increase at aging temperatures despite having a similar microstructure and solute content (C, N are typically linked to DSA [52]) compared with ST. H1150 showed no strength increase at aging temperatures

either. The martensite in H1150 is more extensively tempered compared to H900, which may reduce C and N solute levels from the precipitation of carbides or nitrides. Lower solute levels may reduce the likelihood of DSA in H1150 compared to H900. However, that H900 fails to exhibit DSA effects under very similar test conditions suggests that the strengthening observed in ST is due to rapid precipitate growth. Precipitate growth kinetics measurements, presented later, confirm the plausibility of this hypothesis.

While rapid aging in ST increases its strength and strain hardening, H900 can also soften as precipitates coarsen in the over-aging temperature range. Such effects can occur in a matter of seconds [11]. The two effects combined in our experiments to essentially eliminate any differences in the mechanical behavior of wrought ST and H900 above about 600 °C, despite the very significant differences observed at lower temperatures. By contrast, over-aged (H1150) material was distinctly different than either ST or H900. It exhibited very stable thermal softening and strain hardening through the aging temperature range. Thermal softening remained almost unchanged through the austenite transition temperature, while the strain hardening increased slightly. Precipitate strengthening is often regarded in classical plasticity theory as a strengthening component that augments the strength of the matrix microstructure [1]. The present experimental results show that precipitate strengthening developed by the H900 heat treatment becomes ineffectual above 600 °C. At this point, when the precipitate strengthening component is reduced to zero, the material strength is determined solely by the matrix microstructure. This concept will be used later to construct a time-dependent strength model for 17-4 that depends on precipitate growth kinetics and temperature effects on precipitate strength. For now, it is useful to propose the following conclusion from the experimental data. The matrix strengths of ST and H900 are apparently similar, with the large material strength difference seen at low temperatures ascribable to strong precipitates and the negligible material strength difference seen at high temperatures ascribable to the gradual elimination of the precipitate strengthening effect, via mechanism(s) that are not yet clear but that depend on temperature. If this conclusion is correct, it implies that the peak-aging heat treatment does not significantly alter the matrix microstructure (martensite), as otherwise the strength of ST and H900 would continue to differ once the precipitate strength is reduced to zero. Further, the fact that H1150 differs from ST and H900 suggests that, by contrast, the over-aging heat treatment alters the martensite matrix in a significant way, causing it to behave differently than ST and H900 even into the austenite region. This conclusion aligns with the previous EBSD and HEXRD results which showed strong similarities between ST and H900 but showed higher austenite levels in H1150. Other solid-state reactions (tempering, for example) reported for over-aged 17-4, though not revealed by the microstructural measurements on hand, likely contribute as well. The foregoing results point to the importance of determining the age-hardening kinetics in wrought ST and AM 17-4 N, particularly at short heating times, to compare with the amount of age-hardening observed during the rapidly-heated Kolsky experiments. Such data are also needed to construct a time-dependent strength model for this alloy suitable for dynamic plasticity problems. The kinetics of over-aging, where precipitates coarsen and lose coherency, are also of interest, and will be explored later in the paper.

Aging Kinetics of Wrought ST and AM 17-4 N

Room-temperature Kolsky bar tests on wrought ST and AM 17-4 N specimens aged at different temperatures and times are shown in Figs. 6 and 7. Figure 6a shows that age hardening in wrought ST is rapid, with measurable strengthening occurring at all three aging temperatures in less than one second. Peak strength occurred after only 10 s of aging at the intermediate aging temperature (564 °C ± 10 °C) and below 1 s at the highest aging temperature 663 °C ± 9 °C, although the actual peak strength at this aging temperature is highly uncertain given the extremely fast kinetics and the limited data for heating times on the order of 1 s. In Fig. 6b, the wrought ST aging data are normalized by the apparent peak strengths at each aging temperature according to Eq. 5:

$$X = \frac{\sigma_{t,T} - \sigma_{ST}}{\sigma_{peak} - \sigma_{ST}} \tag{5}$$

where $\sigma_{t,T}$ is flow stress measured after aging for time t and temperature T, σ_{ST} is the flow stress of unaged (solution-treated, ST) material, σ_{peak} is the peak flow stress for a given temperature, and X is the fraction of peak flow stress for the particular aging condition. The normalized aging data are plotted in Fig. 6b. They compare very well with hardness-based aging data on wrought 17-4 reported in the literature [11].

The maximum age-hardenability of AM 17-4 N was smaller compared to wrought ST in Kolsky bar tests (176 MPa vs. 450 MPa at 0.075 plastic strain), but the aging kinetics were similar, as shown in Fig. 7. The reduced age-hardenability of AM 17-4 N relative to wrought ST may have several causes. Aging reactions in metastable austenite are unstudied, therefore the influence of large amounts of austenite on the precipitation reaction is a matter of speculation. First, precipitates formed in austenite would likely be coherent with the FCC matrix, thus their strengthening effect may be quite different than the coherent precipitates grown in martensite. Second, the driving force for precipitation in austenite is lower than in martensite because due to differences in copper solubility,

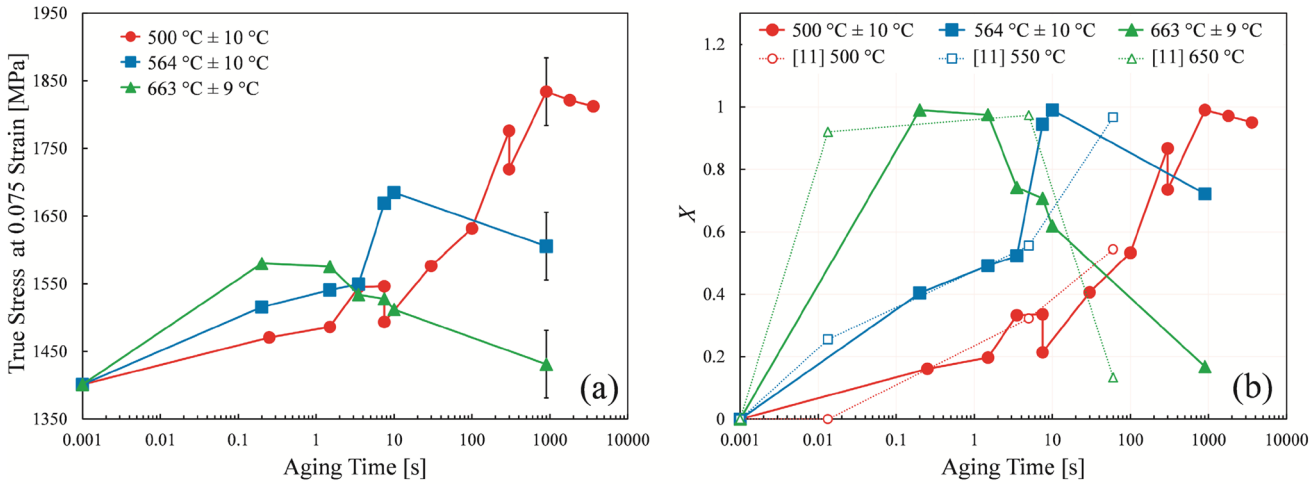

Fig. 6 Aging experiments on wrought ST at various temperatures performed with room temperature Kolsky bar tests ($\dot{\varepsilon} \approx 2\ 000$ 1/s), plotted in terms of flow stress (**a**) and aging fraction X (**b**). Aging fraction data are compared with literature results based on hardness measurements [11]

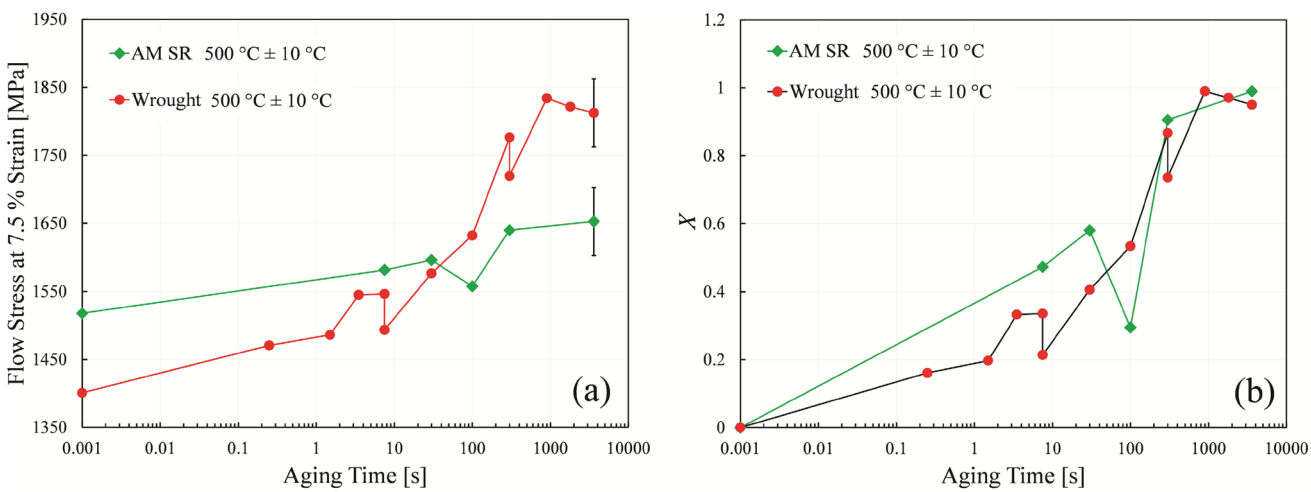

Fig. 7 Aging experiments of AM 17-4 N using room temperature Kolsky bar tests ($\dot{\varepsilon} \approx 2\ 000$ 1/s) plotted in terms of flow stress (**a**) and aging fraction X (**b**). Wrought ST results from Fig. 6 are shown for comparison

so a smaller precipitate volume fraction and lower hardenability might be expected in austenite [11]. Finally, any precipitation that occurs during the build process [53] or stress-relief aging treatment will reduce the amount of available copper for forming additional precipitates, thereby reducing the potential for further age-hardening.

Modeling the Time-dependent Dynamic Mechanical Behavior of Wrought 17-4 in the Solution-treated Condition

Plasticity Model for Wrought 17-4 ST

We now develop a plasticity model to capture the time-dependent plastic behavior of wrought 17-4 in the solution-treated condition due to copper precipitate formation at aging temperatures. This model is also used here to extract aging kinetics parameters from dynamic stress-strain curves of aged samples. The plasticity model considers the strength of 17-4 as the sum of the martensite matrix strength, which is considered sensitive to both temperature and strain-rate, and a precipitate strengthening term, which depends on aging temperature and aging time.

Martensite strength (σ_M) is modeled with a modified form of the Johnson–Cook (JC) plasticity model [54] to which a precipitate strengthening term ($\sigma_{precipitates}$) is added to determine the overall material strength, σ:

$$\sigma = \sigma_{\mathrm{M}} + \sigma_{\mathrm{precipitates}} \tag{6}$$

The basic JC plasticity model combines individual functions accounting for strain, strain rate and temperature effects on flow stress, denoted in Eq. 7 as g, h and j, respectively. This model is here modified to allow the strain rate to influence the strain hardening behavior, which was observed in the experiments:

$$\sigma_{\mathrm{M}} = g(\varepsilon,\ \dot{\varepsilon})h(\dot{\varepsilon})j(T) \tag{7}$$

A two-parameter strain rate sensitivity function is implemented to account for the increase in sensitivity observed at high strain rates in BCC metals [55]:

$$h(\dot{\varepsilon}) = \left(1 - c_1\left(1 - \left(\frac{\dot{\varepsilon}}{\dot{\varepsilon}_{\mathrm{ref}}}\right)^{c_2}\right)\right) \tag{8}$$

Strain hardening is made sensitive to strain rate using a relationship similar to Eq. 9 but with slightly modified fit coefficients:

$$g(\varepsilon, \dot{\varepsilon}) = \left(A_{\mathrm{M}} + \left(B_{\mathrm{M}} * h_2(\dot{\varepsilon})\right)\varepsilon^{n_{\mathrm{M}} * h_2(\dot{\varepsilon})}\right) \tag{9}$$

In Eq. 9, h_2 has the same form as h in Eq. 8 but with c_1 replaced by $F{*}c_1$. F modifies the first strain rate sensitivity coefficient (c_1) to better fit the strain hardening data. The temperature sensitivity function is unchanged from the original JC model:

$$j(T) = \left(1 - \left[\frac{T - T_{\mathrm{ref}}}{T_{\mathrm{melt,M}} - T_{\mathrm{ref}}}\right]^{m_{\mathrm{M}}}\right) \tag{10}$$

In Eqs. 9 and 10, the subscript M denotes martensite, to distinguish from the similar coefficients associated with the precipitate strength term, which is described next. In Eq. 10, $T_{\mathrm{melt,M}}$ is the martensite melting temperature and T_{ref} is a reference temperature, here 23 °C.

Two precipitate strengthening models are explored. The first, simpler approach, considers precipitate strengthening to be independent of temperature, e.g. precipitates represent an athermal barrier to plastic flow. Strain and strain rate hardening effects due to precipitates are similarly ignored, so that the strengthening effect is reduced to a stress factor that depends only on prior aging time and temperature. In the second model, the precipitate strength is allowed to vary with temperature and to influence the strain hardening but not the strain rate hardening. The latter assumption follows from the previous experimental results that show only a minor influence of precipitate strength on the rate sensitivity of wrought 17-4 (Fig. 4). The time-dependence of the age-hardening effects is captured with an aging kinetics model, described next.

Aging Kinetics Model for Wrought 17-4 ST

Aging kinetics in 17-4 are modeled using the global analysis method developed in [11], referred to as the JMAK (Johnson–Mehl–Avrami–Kolmogorov) - Arrhenius analysis. We note that the applicability of this method has been questioned in the literature because it does not account for the effect of solute consumption on continuous precipitate growth [56]. Further, because the extent of the precipitate growth is determined indirectly via Kolsky bar testing rather than directly by measuring precipitate population characteristics (size and distribution), the model will possibly also include other microstructural effects associated with aging, such as martensite tempering and/or austenite reversion. We further note that this model captures hardening on aging, but not softening on over-aging (as shown previously in Fig. 6). The aging kinetics model is given by:

$$X = \frac{\sigma_{\mathrm{t,T}} - \sigma_{\mathrm{ST}}}{\sigma_{\mathrm{peak}} - \sigma_{\mathrm{ST}}} = 1 - \exp\left(\left(-k_0 \exp\left(-\frac{Qz}{RT_{\mathrm{aging}}}\right)\right)(t^z)\right) \tag{11}$$

where X is defined as before, k_0 is the reaction rate pre-exponential, Q is the apparent activation energy, R is the gas constant (8.314 J/(mol K)) and z is the precipitate growth exponent. As demonstrated by the aging experiments, σ_{peak} is temperature-dependent (Fig. 6), and this is accounted for by an empirical interpolation factor given by:

$$\sigma_{\mathrm{peak}} - \sigma_{\mathrm{ST}} = \left(\sigma_{\mathrm{peak,\ H900}} - \sigma_{\mathrm{ST}}\right) * \left(y_0 + y_1 T_{\mathrm{aging}} + y_2 T_{\mathrm{aging}}^2\right) \tag{12}$$

Here $\sigma_{\mathrm{peak,H900}}$ is the peak strengthening for the H900 condition as observed at room temperature (the maximum age-hardening level in this alloy), and the term $\left(y_0 + y_1 T_{\mathrm{aging}} + y_2 T_{\mathrm{aging}}^2\right)$ is a unitless empirical function that reduces the peak aging strength value when T_{aging} exceeds 900 °F (482 °C), e.g. $\sigma_{\mathrm{peak,\ H(T>900)}} < \sigma_{\mathrm{peak,\ H900}}$.

For the simplified precipitate strength model, the precipitate strength depends on t_{aging} and T_{aging} through the kinetic function X and through the interpolation function f that reduces peak-aged strength with increases in T_{aging}:

$$\sigma_{\mathrm{precipitates}} = \sigma_{\mathrm{t,T}} - \sigma_{\mathrm{ST}} = \left(\sigma_{\mathrm{peak,H900}} - \sigma_{\mathrm{ST}}\right) f\left(T_{\mathrm{aging}}\right) X\left(t_{\mathrm{aging}}, T_{\mathrm{aging}}\right) \tag{13}$$

In the above equation, $\sigma_{\mathrm{t,T}} - \sigma_{\mathrm{ST}}$ represents the net precipitate strengthening as determined by subtracting the flow stress of material age-hardened at different temperatures and times $\left(\sigma_{\mathrm{t,T}}\right)$ from un-aged material $\left(\sigma_{\mathrm{ST}}\right)$ obtained from room temperature Kolsky bar tests. We note that this model ignores any loss in solid-solution strengthening that may occur as copper is removed from solution to form the precipitates. The model also assumes that the martensite matrix is otherwise unaffected by aging (tempering or austenite

reversion, for example) such that σ_M can be fully specified by fitting wrought ST data at low temperatures (< 400 °C) and extrapolating the result up through aging temperatures.

In the second, more complex precipitate strength model, the precipitate strength term is allowed to vary with temperature and strain by employing a separate JC equation for the precipitate strength, replacing the previous, constant strength factor that depended only on aging temperature and aging time. This new precipitate model is combined with the previous kinetics model for precipitate growth as before (Eq. 13):

$$\sigma_{\text{precipitates}} = \sigma_{\text{t,T}} - \sigma_{\text{ST}} = \left(A_{\text{p}} + B_{\text{p}}\varepsilon^{n_{\text{p}}}\right) \left(1 - \left[\frac{T - T_{\text{ref}}}{T_{\text{m,p}} - T_{\text{ref}}}\right]^{m_p}\right) f\left(T_{\text{aging}}\right) X\left(t_{\text{aging}}, T_{\text{aging}}\right) \quad (14)$$

In Eq. 14, the subscript p on each fit coefficient denotes precipitates to distinguish them from the fit coefficients that describe the martensite matrix. The precipitate model uses the same strain hardening and thermal softening functions employed in the original JC model, unlike the martensite matrix strength model. $T_{\text{m,p}}$ is the effective "melting" temperature of the precipitates, here taken as the solutionizing temperature (1050 °C), where the precipitates are fully dissolved in the austenite matrix, given sufficient time.

All parameters were fit by minimizing relevant objective functions using the Nelder-Mead method [57] available in the SciPy Python library [58]. Averaged stress-strain curves were used for fitting room temperature experiments, when available, while high temperature experiments were fit as individual experiments. Averaged stress-strain curves were weighted higher than individual experiments in proportion to the number of replicates available for fitting. Model fits used the average strain rates measured experimentally for each individual stress-strain curve or averaged stress-strain curve.

Fit coefficients for the equations that determine σ_M and $\sigma_{\text{precipitates}}$ are found as follows. First, the strength coefficients for σ_M (A_M, B_M, n_M, m_M, c_1, c_2 and F) are determined from wrought ST data at different strain rates and temperatures up to 400 °C. Next, $\sigma_{\text{peak,H900}}$ is determined by fitting room-temperature dynamic H900 data using Eq. 13 for the simple precipitate model. The complex precipitate model is obtained by fitting A_p, B_p, n_p and m_p in Eq. 14 using H900 stress-strain data at temperatures up to 400 °C. Recall that the H900 condition represents the strongest peak aged condition, for which $f(T) \approx 1$ and $X = 1$. Next, coefficients for $f\left(T_{\text{aging}}\right)$ are determined by fitting peak-aged data obtained at different aging temperatures (Fig. 6a) in the same manner, with $T = T_{\text{ref}}$, $X = 1$ and $f(T)$ taking on values less than unity for aging temperatures higher than 500 °C. We note here that the $f(T_{\text{aging}})$ fit relies on accurate peak strengths at high aging temperatures, which are in practice difficult to determine due to their very fast kinetics, as previously mentioned. This aspect of the strength model therefore has significant uncertainty. Finally, the kinetics parameters k_0, Q and z are fit using the room-temperature dynamic stress-strain data on ST samples aged at different temperatures and times. The more complex (strain-dependent) precipitate strength model is used (Eq. 14) to extract these kinetics parameters from the dynamic stress-strain data.

Separate fits to the data in the austenite region are made using Eq. 8, assuming the same strain rate sensitivity parameters used for the martensite.

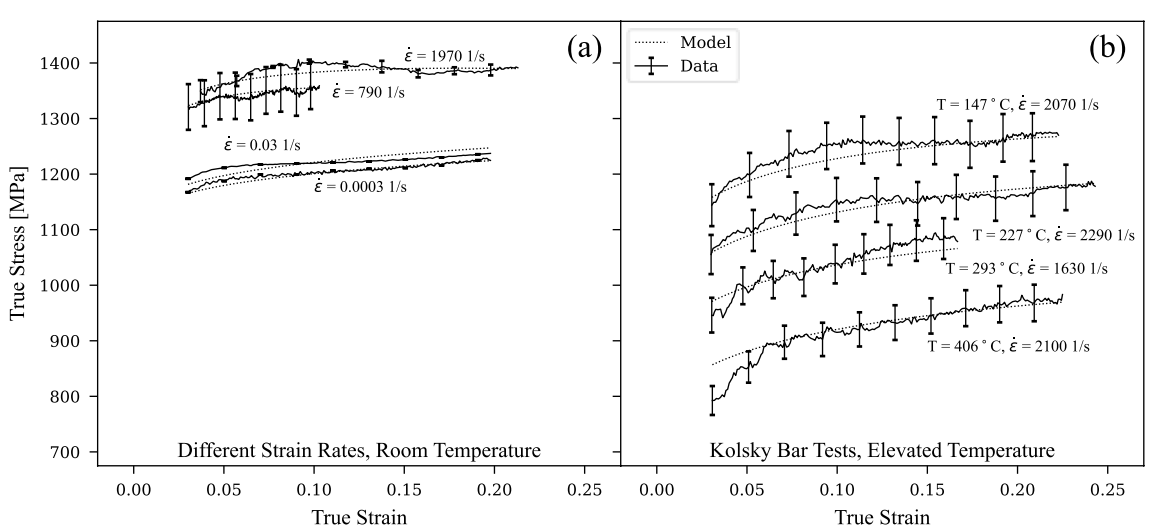

Fig. 8 Model fit of wrought ST 17-4 at various strain rates and room temperature (**a**) and high strain rates for temperatures up to 400 °C (**b**)

Plasticity Model for Wrought 17-4 in the H1150 Condition

To complete the analysis of wrought 17-4, a separate plasticity model is determined for wrought H1150, which behaves differently than wrought ST and H900, likely due to the martensite tempering and austenite reversion that occurs during the extended high temperature heat treatment. Because the precipitates can be expected to remain relatively stable under rapid heating, no time-dependent kinetics terms are thought necessary. Even if these precipitates were to evolve on heating, their relatively low strengthening effect will tend to make any such changes difficult to detect in Kolsky bar tests. The H1150 strength model is based on the basic JC model with the modified strain rate factor used previously for the ST strength model. However, the H1150 model differs in two ways from the ST model. First, because the strain hardening in H1150 decreased with temperature (Fig. 5), a temperature factor is added to the strain hardening parameter to account for this behavior [59]. In addition, the strain rate dependence of strain hardening used previously in the ST strength model is not needed. The H1150 model is shown in Eq. 15 below. The fit coefficients are listed in Table 4, and the fit is plotted against the data in Fig. 15.

Table 3 Parameter values of the time-dependent plasticity model for wrought 17–4 ST including simple and complex (temperature- and strain-sensitive) precipitate strength models. Model coefficients for the austenite temperature range (> 750 °C) are also included

σ_M				
A_M [MPa]	B_M [MPa]	n_M	c_1	c_2
987	302	0.151	0.00459	0.237
F	$\dot{\varepsilon}_{ref,M}$ [1/s]	$T_{ref,M}$ [°C]	$T_{melt,M}$ [°C]	m_M
7.09	0.0003	23	1404	0.729
$\sigma_{precipitates}$ (Simple Model)				
$\sigma_{peak,H900} - \sigma_{ST}$[MPa]				
488				
y_0	y_1	y_2		
− 2.14	0.0126	− 0.000013		
k_0	Q	z		
502	142	0.322		
$\sigma_{precipitates}$ (Temperature- and Strain-Sensitive Model)				
A_p [MPa]	B_p [MPa]	n_p	m_p	$T_{melt,p}$ [°C]
0	822	0.232	1.01	1050
y_0	y_1	y_2		
− 2.59	0.0144	− 0.0000147		
k_0	Q [kJ/mol]	z		
507	148	0.314		
$\sigma_{Austenite}$				
A_A [MPa]	B_A [MPa]	n_A	c_1	c_2
369	332	0.165	0.00459	0.237
F	$\dot{\varepsilon}_{ref,A}$ [1/s]	$T_{ref,A}$ [°C]	$T_{melt,A}$ [°C]	m_A
7.09	0.0003	23	1404	1.03

Table 4 Model coefficients for the plastic behavior of wrought 17-4 in the H1150 condition

$\sigma_{Austenite}$				
A_A [MPa]	B_A [MPa]	n_A	c_1	c_2
369	332	0.165	0.00459	0.237
F	$\dot{\varepsilon}_{ref,A}$ [1/s]	$T_{ref,A}$ [°C]	$T_{melt,A}$ [°C]	m_A
7.09	0.0003	23	1404	1.03

$$\sigma = \left(A + B\left(1 - \left[\frac{T - T_{ref}}{T_m - T_{ref}}\right]^m\right)\varepsilon^n\right)\left(1 - c_1\left(1 - \left(\frac{\dot{\varepsilon}}{\dot{\varepsilon}_{ref}}\right)^{c_2}\right)\right)\left(1 - \left[\frac{T - T_{ref}}{T_m - T_{ref}}\right]^m\right) \tag{15}$$

In the above equation, a single value of m governs both thermal softening and the temperature effect on strain hardening. In the previous implementation of this model approach, two different values are used for thermal softening and temperature-modified strain hardening [59].

Model Results and Discussion

Parameter values for the martensite matrix strength of wrought ST material, σ_M, and for the precipitate strength, $\sigma_{precipitates}$, for both precipitate models, are listed in Table 3. Parameter values for the H1150 strength model are listed in Table 4. Recalling that the parameter values for σ_M are determined by fitting low temperature ST data (prior to any age-hardening), the resulting martensite strength model is compared to low temperature experiments in Fig. 8. As previously discussed, adiabatic heating is calculated with Eq. 4 and is assumed to occur for strain rates higher than 1.0 1/s [1].

In Fig. 9, the global kinetics model fit is compared to the aging data taken at a strain of 0.075 as before. The plot variables are determined based on Eq. 16 below, which is a re-arranged form of Eq. 6 for a given value of Q and T_{aging}:

$$\ln(k) + z\ \ln(t) = \ln\left(\ln\left(\frac{1}{1 - X}\right)\right) \tag{16}$$

where $k = k_0 exp\left(-\frac{Qz}{RT_{aging}}\right)$. In this form, the re-arranged aging fraction parameter, $\ln\left(\ln\left(\frac{1}{1-X}\right)\right)$, is linear in $\ln(t)$,

with slope z and intercept ln(k). This plotting method conveniently demonstrates how the global kinetic fit approach is able to capture the entire aging data set despite its previously noted limitations [11]. Figure 10 plots the kinetic fit against several selected room temperature dynamic stress-strain curves for wrought ST specimens aged at different temperatures and times up to the peak aged condition. Unlike Fig. 9, this plot reveals how the strain hardening increases upon aging for each aging temperature investigated.

Figure 11 compares the model predictions for both precipitate models into the aging temperature range against elevated-temperature Kolsky bar data replotted from Fig. 5. Both models are evaluated for heating times of 0 s (no aging), 3.5 s, and 60 s, with aging considered to occur entirely at the initial test temperature of a given experiment. The models are also evaluated for a heating time of 3600 s at 482 °C, representing the H900 condition. Again, this model condition does not account for precipitate coarsening that may occur in H900 at high temperatures, which may tend to reduce the material strength. This effect is analyzed later. The models are also evaluated for no heating time (the 0 s case), which is simply an extrapolation of the low temperature behavior of the martensite matrix, σ_M, into the aging temperature range with no precipitate growth. It is apparent that the athermal precipitate strength model (Fig. 11a) significantly overestimates the amount age hardening expected for wrought ST during the Kolsky bar tests compared to experiment. Moreover, the athermal precipitate strength model begins to over-predict the H900 flow stress starting near 300 °C and becomes progressively worse thereafter. Thus, the strength of H900 is more sensitive to temperature compared to the sum of the martensite matrix strength and the athermal precipitate strengthening contribution determined at room temperature, even at temperatures well below those where precipitate coarsening would be expected (< 500 °C). Therefore, the precipitate strengthening mechanism in this alloy is apparently temperature-sensitive at dynamic strain rates, e.g., the copper precipitates in this alloy do not act as athermal barriers to plastic flow. Quasi-static test data reported in the literature also indicate that aged 17-4 softens more quickly with temperature compared to solution-treated 17-4 below 500 °C [9]. The more complex precipitate model with strain- and temperature-dependent precipitate strengthening provides much better predictions of the data at aging temperatures (Fig. 11b). An important consequence of the temperature sensitivity of precipitate strengthening is that it greatly reduces the magnitude of the time-dependent strengthening in wrought ST that might otherwise have been expected. Finally, because the ST and H900 data are basically indistinguishable in the austenite range, data for both materials are combined and used to determine the austenite strength fit considering matrix behavior alone (Eq. 7). The fit is included in Fig. 11. We also note that

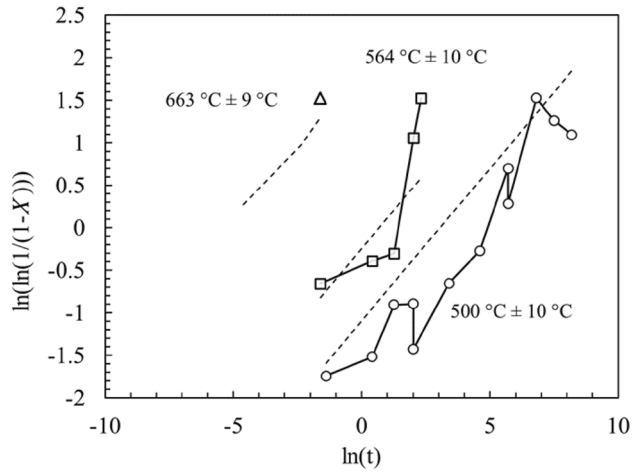

Fig. 9 Global aging kinetics fit for wrought ST up to peak aging. For the aging experiments conducted at 663 °C, the peak strength occurred at the shortest possible aging time (0.2 s). Symbols are experimental data and dashed lines are the model fit results evaluated at each average aging temperature

this fit ignores the possibility of precipitate growth in austenite under rapid heating. Also, this austenite model fit retains the strain rate sensitivity of martensite determined previously at room temperature, which is unlikely to be the case.

Figure 12 compares the temperature and strain-dependent precipitate strength model against the full dynamic stress-strain curves for wrought ST and H900. These plots give a more detailed picture of the agreement between the model and the stress-strain data compared to what was shown previously in Fig. 11. The model predictions for wrought ST above 400 °C are fairly good up to just below the austenite transition, although the agreement is poor for the highest experimental temperature (689 °C ± 41 °C), where the model significantly over-predicts the strength. As previously noted, the thermal softening of both ST and H900 seems to accelerate below the nominal austenite transformation temperature of 750 °C, which indicates the actual austenite transformation temperature may be lower despite the rapid heating used in these experiments, which ought to increase Ac1 rather than decrease it. This issue is left to future work. Turning to the H900 predictions, as discussed already, the model significantly over-predicts the strength in the over-aging range (550 °C to Ac1). Austenite transition is not expected at these temperatures. Rather, particle coarsening effects, which are not included in the model, may contribute to the poor predictions of H900 strength in the over-aging regime. Finally, the martensite-to-austenite transition has a significant effect on wrought ST and H900, which behave identically near the austenite transition and above, and this transformation may also be time-dependent, for short heating times. This is also left to future study.

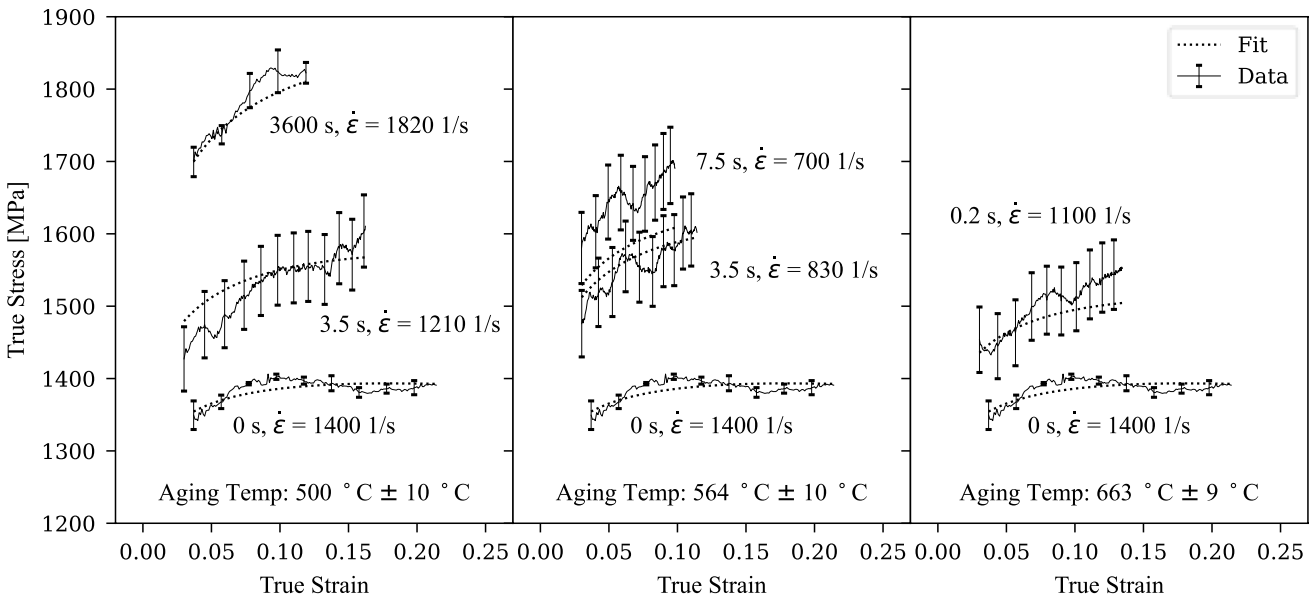

Fig. 10 Selected room temperature dynamic stress-strain curves of wrought ST aged at different temperatures and times with model fits. The 0 s heating data and fit represents the average dynamic stress-strain curve for wrought ST with no additional aging

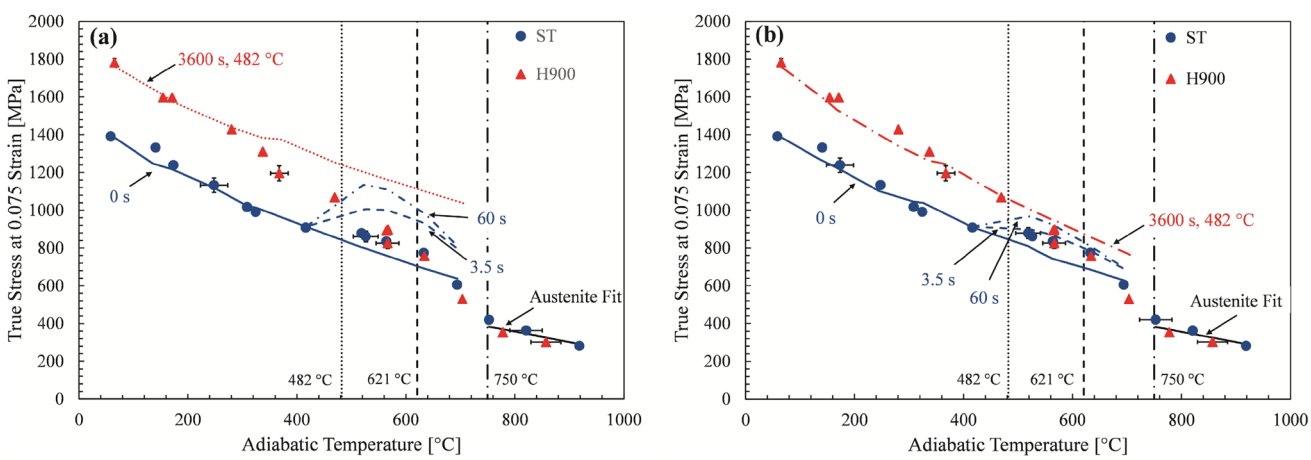

Fig. 11 Time-dependent plasticity models versus data for (**a**) precipitate strengthening independent of temperature and strain (Eq. 13) and (**b**) precipitate strengthening with temperature and strain dependence (Eq. 14). Peak-aged (H900) data are included for comparison. Austenite region fits are also shown

As previously noted, coarsening of precipitates in H900 is known to reduce the material's strength upon re-heating to high temperatures (e.g. over-aging treatments) [9]. Coarsening effects were explored in wrought H900 by subjecting samples to additional rapid (3.5 s, heating profile similar to Fig. 1a) over-aging heat treatments at temperatures between 500 and 930 °C, followed by quenching and then room temperature dynamic testing. This same procedure was used previously for the aging experiments on wrought ST. Figure 13a shows the strength (in MPa) of H900 after rapid over-aging treatments while Fig. 13b plots the relative strength loss compared to the peak-aged condition (X from Eq. 6) versus aging temperature. The relative strength loss data again compare well with literature data based on hardness tests [11]. The present coarsening data are fit with a linear model (shown in Fig. 13a) and this model is used to calculate the strength loss due to coarsening that might be expected in the elevated-temperature Kolsky bar tests on H900. As the linear model estimates the strength loss at room-temperature, it must be modified by the precipitate temperature sensitivity factor, $\left(1-\left[\frac{T-T_{\mathrm{ref}}}{T_{\mathrm{m,p}}-T_{\mathrm{ref}}}\right]^{m_{\mathrm{p}}}\right)$, from

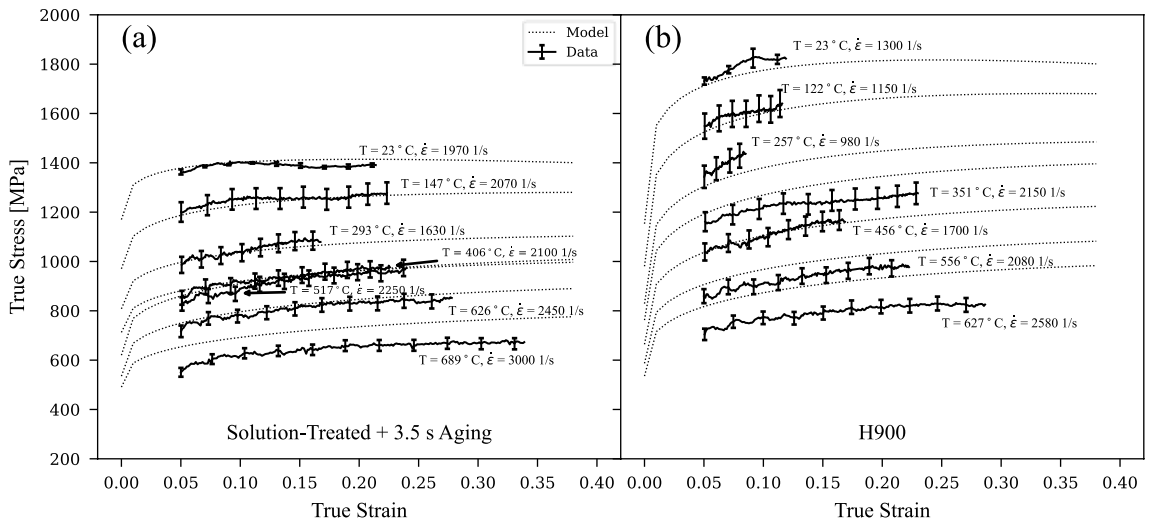

Fig. 12 Time-dependent plasticity model for wrought ST with precipitate strengthening sensitive to temperature and strain (Eq. 14) versus (**a**) wrought ST experiments and (**b**) wrought H900 experiments

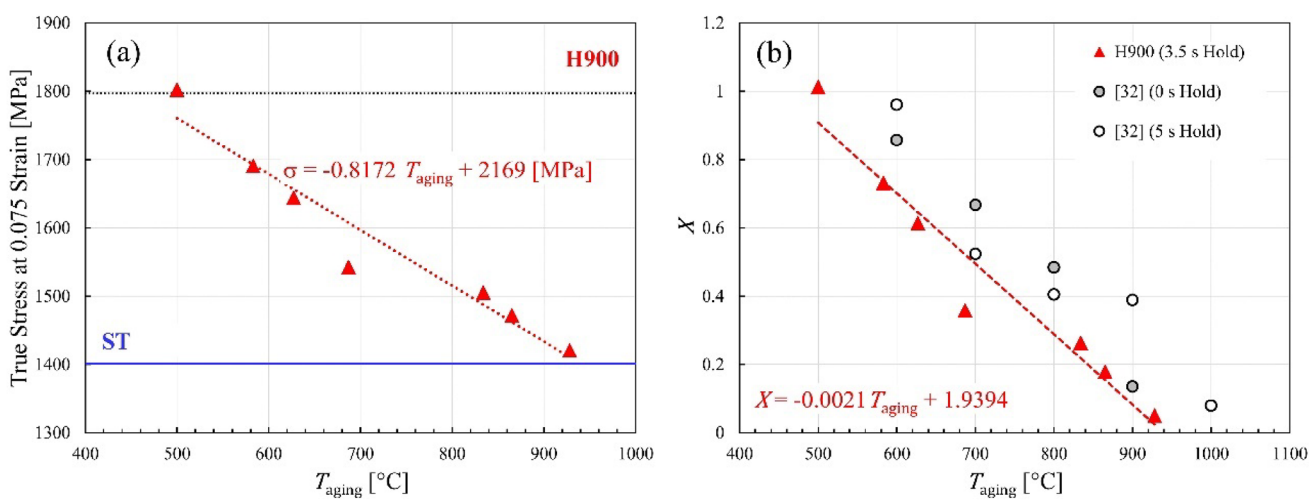

Fig. 13 Rapid aging experiments on H900 (3.5 s aging time followed by quench to room temperature) expressed in MPa at 0.075 strain (**a**) and aging fraction X (**b**), the latter compared with hardness measurements of rapidly-aged H900 reported in the literature [11]. The horizontal lines in (**a**) indicate the maximum (H900) and minimum (ST) strength levels to contextualize the relative strength loss experienced by H900 after aging

Eq. 14, to estimate the magnitude of the strength loss experienced at elevated temperatures.

Figure 14 compares the estimated strength loss due to precipitate coarsening from the H900 aging experiments (Fig. 13) against the magnitude of the model discrepancy with H900 data in the over-aging temperature range (Figs. 11 and 12). Recall that the strength model is based on the low-temperature (< 400 °C) thermal softening behavior of H900 (matrix plus precipitates), where the precipitate population is presumably stable with respect to heating. The model prediction rapidly worsens for temperatures above 550 °C, and as Fig. 14 shows, precipitate coarsening explains much of the additional thermal softening observed in the experiments for temperatures below about 600 °C. At higher temperatures, however, coarsening does not fully explain the difference between the strength model and the H900 data. One possibility is that the precipitate strengthening mechanism is increasingly temperature-sensitive in the over-aging range compared with lower temperatures, independent of coarsening, such that a yet more complex thermal softening model is needed for the precipitates in this alloy. Another possibility is that that austenite transformation begins at a lower-than-expected temperature, which would tend to

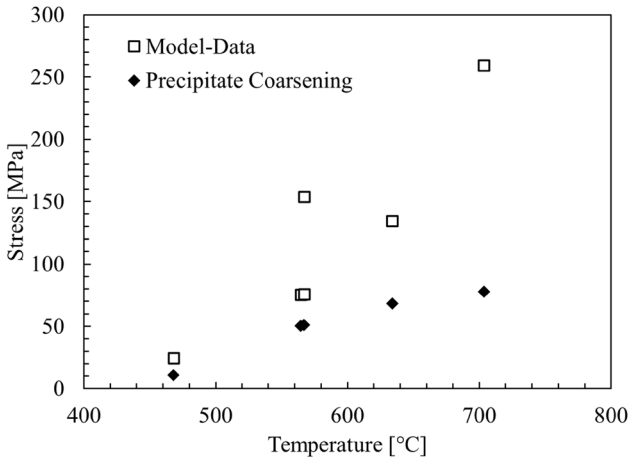

Fig. 14 Difference between the predicted and measured flow stress of H900 in elevated-temperature Kolsky bar tests (Figs. 11 and 12), evaluated at 0.075 strain (Model-Data) and the expected strength loss due to precipitate coarsening estimated from H900 aging tests (Precipitate Coarsening, Fig. 13)

increase the apparent thermal softening rate. However, the austenite transition temperature should increase under rapid heating compared to the equilibrium value of about 750 °C, so this would be an unexpected result. Direct observations of the evolving precipitate population with temperature and time near Ac1 are needed to explore the issue further.

Figure 15 compares the strength model fit for wrought H1150 (Eq. 15, Table 4) against the data up to almost 900 °C. The model adequately captures the data at all strain rates and temperatures, and its precipitate population is assumed to be stable under rapid heating and therefore requires no account of either rapid growth or coarsening on heating.

Evidence of Aging in am 17-4 N

Following previous discussions, the high strength of AM 17-4 N relative to wrought ST, combined with high strain hardening at low temperatures, may in some ways exceed wrought material in terms of toughness, for example. However, as the underlying causes for its high strength are unknown, weighing possible benefits should be done with caution. As discussed, the large amount of austenite in AM 17-4 N ought to reduce its strength compared to fully martensitic wrought material. EDS measurements revealed the absence of Nb(C,N) in AM 17-4 N, which is understandable given the thermal history during the AM process is not conducive to their growth. Their absence may enhance the solid solution strengthening effects of C and N in martensite, with N concentrations exceeding wrought levels based on chemical analysis. Additional strengthening via copper precipitation during the stress relief heat treatment process or the build process itself is also suspected. To investigate this latter possibility, AM 17-4 N samples were subjected to rapid austenitizing (RA) treatments like those performed on H900 to eliminate pre-existing age-hardening effects. RA treatments were performed at approximately 900 °C with a 3.5 s heating time and a heating profile similar to Fig. 1a, followed by quenching in the Kolsky bar. Figure 16 shows that the average strength of AM 17-4 N decreased almost 300 MPa after the RA treatment, confirming significant prior age-hardening existed in this AM material. The strain hardening remained high after the RA treatment, indicating that austenite is probably retained despite the austenitizing-then-quenching treatment, although this was not independently confirmed by HEXRD measurements. Slightly higher carbon, nickel,

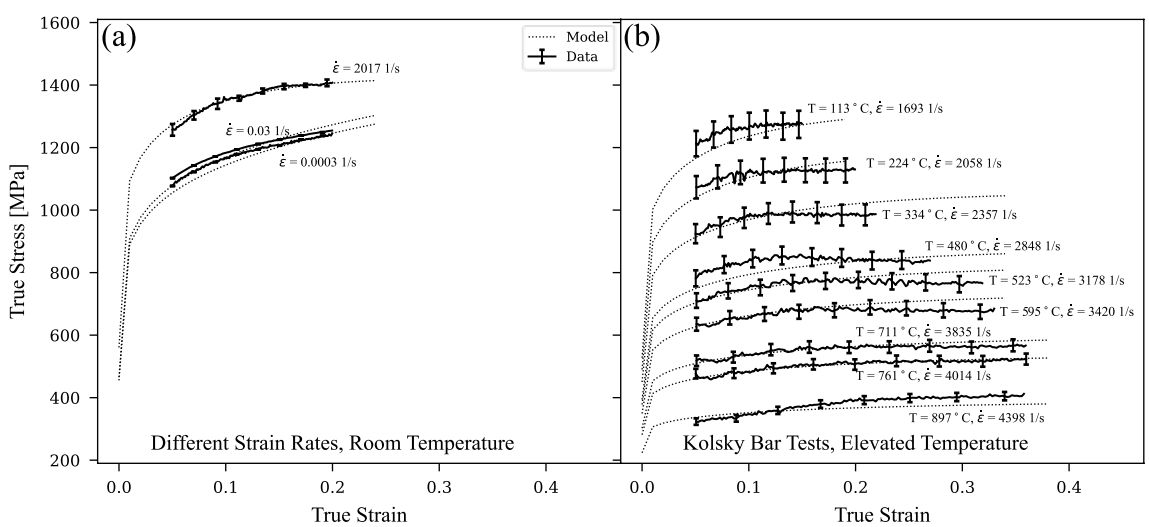

Fig. 15 Strength model for wrought H1150 versus stress-strain data at different strain rates (**a**) and at different temperatures for high strain rates (**b**)

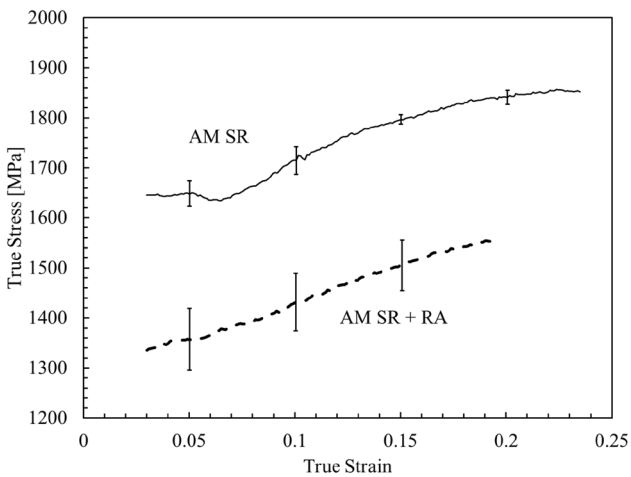

Fig. 16 The effect of rapid austenitizing (RA) experiments on the dynamic behavior of AM 17-4 N. Each curve is the average of five experiments

copper and oxygen levels in this material compared to wrought may provide additional solid solution strengthening or oxide dispersion strengthening.

Conclusions

This work investigated both wrought and AM-produced 17-4 martensitic stainless steels, where substantial hardenability via copper precipitation makes this alloy system a prime candidate to exhibit time-dependent plastic behavior relevant to dynamic problems such as machining and impact response. Wrought 17-4 was examined in the solution-treated (ST), peak-aged (H900) and over-aged (H1150) conditions using a rapidly-heated Kolsky bar technique at temperatures up to 1000 °C and heating times ≈ 3 s. AM 17-4 N was examined only in the stress-relieved condition. Rapid aging in ST caused thermal hardening at aging temperatures (> 400 °C), but the magnitude of the hardening was significantly reduced by the temperature-sensitivity of the precipitate strengthening mechanism. At higher aging temperatures (> 600 °C), rapid precipitate coarsening contributed to the strength loss observed in age-hardened material. A plasticity model was constructed for wrought ST that includes time-, temperature-, and strain-dependent precipitation strengthening. A separate model was developed for H1150, whose strength characteristics were quite different from the other two wrought materials likely due to over-aging effects on the martensite matrix. Additional conclusions are:

- AM 17-4 N exhibits high room-temperature strength and high strain hardening due to a large meta-stable austenite content (27% volume fraction via HEXRD) and a significant amount of age-hardening that occurs during the build or stress-relief heat treatment process. These characteristics will likely result in poorer machinability relative to wrought 17-4 in the ST or H1150 conditions.
- Wrought 17-4 displays positive room temperature strain rate sensitivity for all heat treatment conditions, in accord with its martensitic structure. AM 17-4 N displays complex strain rate sensitivity due to its large metastable austenite content.
- The precipitate strengthening kinetics of wrought ST and AM 17-4 N are similar but AM 17-4 N is significantly less hardenable due to prior aging during the build and/or SR heat treatment.
- Wrought ST and H900 behave identically in Kolsky bar tests conducted at and above 600 °C, but distinctly from over-aged (H1150) in this range, suggesting that the peak-aging heat treatment has very little effect on the martensite matrix while the over-aging heat treatment has a significant effect on it. This observation correlates well with microstructural analysis presented in this paper and the more extensive microstructural analyses available in the literature.

Acknowledgements The authors gratefully acknowledge input from Mark R. Stoudt, Michael Katz, Sandy Young and Adam Creuziger at NIST during the course of this work. We also thank Dr. Jun-Sang Park for his help with the HEXRD measurements. This research used resources of the Advanced Photon Source, a U.S. Department of Energy (DOE) Office of Science user facility operated for the DOE Office of Science by Argonne National Laboratory under Contract No. DE-AC02-06CH11357.

Author contribution SM: Experimental design and execution, primary content creator. SH: Experimental design and execution, content editing. JZ: EBSD measurements and analysis, content editing. FZ: HEXRD measurements and analysis, content editing.

Declarations

Conflict of interest The authors have no conflict of interest to declare regarding the content of this manuscript.

References

1. Follansbee PS (2014) Fundamentals of strength: principles, experiment, and applications of an internal state variable constitutive formulation. Wiley
2. Marchand A, Duffy J (1988) An experimental study of the formation process of adiabatic shear bands in a structural steel. J Mech Phys Solids 36(3):251–283
3. Childs TH et al (2000) Metal machining: theory and applications. Butterworth-Heinemann
4. Ludwigson DC, Hall AM (1959) The physical metallurgy of precipitation-hardenable Stainless steels. Battelle Memorial Institute, Columbus, OH, USA, p 68
5. Rack HJ, Kalish D (1974) The strength, fracture toughness, and low cycle fatigue behavior of 17 – 4 PH Stainless Steel. Metall Trans 5:1595–1605
6. Viswanathan UK, Banerjee S, Krishnan R (1988) Effects of Aging on the microstructure of 17 – 4 Ph Stainless-Steel. Mater Sci Eng a-Structural Mater Prop Microstruct Process 104:181–189
7. Murayama M, Katayama Y, Hono K (1999) Microstructural evolution in a 17 – 4 PH stainless steel after aging at 400 degrees C. Metall Mater Trans a-Physical Metall Mater Sci 30(2):345–353
8. Hsiao CN, Chiou CS, Yang JR (2002) Aging reactions in a 17 – 4 PH stainless steel. Mater Chem Phys 74(2):134–142
9. Wu J-H, Lin C-K (2003) Influence of high temperature exposure on the mechanical behavior and microstructure of 17 – 4 PH stainless steel. J Mater Sci 38(5):965–971
10. Mirzadeh H, Najafizadeh A (2009) Aging kinetics of 17 – 4 PH stainless steel. Mater Chem Phys 116(1):119–124
11. Hamlin RJ, DuPont JN, Robino CV (2018) Simulation of the Precipitation Kinetics of Maraging Stainless Steels 17 – 4 and 13 – 8 + Mo during multi-pass welding. Metall Mater Trans A 50(2):719–732
12. Bhambroo R et al (2013) Effect of reverted austenite on mechanical properties of precipitation hardenable 17 – 4 stainlesssteel. Mater Sci Engineering: A 568:127–133
13. Wang Z et al (2018) Nano-precipitates evolution and their effects on mechanical properties of 17 – 4 precipitation-hardening stainless steel. Acta Mater 156:158–171
14. Rowolt C et al (2020) Dissolution and precipitation of copper-rich phases during heating and cooling of precipitation-hardening steel X5CrNiCuNb16-4 (17 – 4 PH). J Mater Sci 55(27):13244–13257
15. Murr LE et al (2012) Microstructures and properties of 17 – 4 PH Stainless Steel fabricated by selective laser melting. J Mater Res Technol 1(3):167–177
16. Cheruvathur S, Lass EA, Campbell CE (2015) Additive Manufacturing of 17 – 4 PH Stainless Steel: post-processing heat treatment to Achieve Uniform reproducible microstructure. Jom 68(3):930–942
17. LeBrun T et al (2015) Effect of retained austenite on subsequent thermal processing and resultant mechanical properties of selective laser melted 17-4 PH stainless steel. Mater Design 81:44–53
18. Merklein M et al (2016) Hybrid additive Manufacturing technologies – an analysis regarding potentials and applications. Physics Procedia 83:549–559
19. Webster S et al (2021) Physical mechanisms in hybrid additive manufacturing: A process design framework. J Mater Process Technol 291:117048
20. Lass EA, Stoudt MR, Williams ME (2019) Additively manufactured Nitrogen-Atomized 17 – 4 PH Stainless Steel with Mechanical Properties comparable to Wrought. Metall Mater Trans A 50(4):1619–1624
21. Freeman FSHB et al (2019) Influence of solidification cell structure on the martensitic transformation in additively manufactured steels. Additive Manuf 30:100917
22. Facchini L et al (2010) Metastable Austenite in 17 – 4 precipitation-hardening Stainless Steel produced by selective laser melting. Adv Eng Mater 12(3):184–188
23. Luecke WE, Slotwinski JA (2014) Mechanical Properties of Austenitic Stainless Steel made by Additive Manufacturing. J Res Natl Inst Stand Technol 119:398–418
24. Clausen B et al (2017) Deformation behavior of additively manufactured GP1 stainless steel. Mater Sci Engineering: A 696:331–340
25. Phan TQ, Kim FH, Pagan DC (2019) Micromechanical response quantification using high-energy X-rays during phase transformations in additively manufactured 17 – 4 stainless steel. Mater Sci Engineering: A 759:565–573
26. Simmons J (1996) Overview: high-nitrogen alloying of stainless steels. Mater Sci Engineering: A 207(2):159–169
27. Fan R et al (2012) Effects of Heat Treatment and Nitrogen on Microstructure and Mechanical properties of 1Cr12NiMo Martensitic Stainless Steel. J Mater Sci Technol 28(11):1059–1066
28. Zhang X et al (2022) Effect of nitrogen and tempering temperature on microstructure evolution and mechanical properties of 0Cr15Ni6Mo2 martensitic stainless steel. Ironmak Steelmak 49(3):311–321
29. Heigel JC et al (2018) Experimental investigation of residual stress and its impact on Machining in Hybrid Additive/Subtractive Manufacturing. Procedia Manuf 26:929–940
30. Childs T et al (2000) In: Childs T et al (eds) 3 - work and tool materials, in Metal Machining. Butterworth-Heinemann: Oxford, pp 81–117
31. Fox C et al (2022) Dynamic constitutive behavior of additively manufactured 17–4PH Stainless Steel. J Dyn Behav Mater. 8(2):242–254
32. Rack H (1981) Physical and Mechanical properties of cast 17 – 4 PH Stainless Steel. NM. Albuquerque, Sandia National Laboratories, p 65. T.T. Center, Editor
33. Gupta C et al (2000) Effect of serrated flow on deformation behaviour of AISI 403 stainless steel. Mater Sci Engineering: A 292(1):49–55
34. Nie Z et al (2016) Phase-based constitutive modeling and experimental study for dynamic mechanical behavior of martensitic stainless steel under high strain rate in a thermal cycle. Mech Mater 101:160–169
35. Nicholas T (1981) Tensile testing of materials at high rates of strain. Exp Mech 21(5):177–185
36. Mates SP et al (2008) A pulse-heated Kolsky Bar technique for measuring the Flow stress of metals at High Loading and Heating Rates. Exp Mech 48(6):799–807
37. Stock SR et al (2019) Precision lattice parameter determination from transmission diffraction of thick specimens with irregular cross sections. J Appl Crystallogr 52(1):40–46
38. Jones EM, Iadicola MA (2018) A good practices guide for digital image correlation. International Digital Image Correlation Society, p 10
39. Gray III, G. and, Blumenthal WR (2000) Split-Hopkinson pressure bar testing of soft materials. ASM Handb 8:488–496
40. Gama BA, Lopatnikov SL, Gillespie JW Jr (2004) Hopkinson Bar experimental technique: a critical review. Appl Mech Rev 57(4):223–250
41. Chen WW, Song B (2010) Split Hopkinson (Kolsky) Bar: design, testing and applications. Springer US
42. Safa K, Gary G (2010) Displacement correction for punching at a dynamically loaded bar end. Int J Impact Eng 37(4):371–384
43. ASTM (1993) Manual on the Use of thermocouples in Temperature Measurement, Fourth Edition, ASTM Manual Series: MNL

12, revision of Special Technical Publication (STP) 470B, in ASTM Manual Series. ASTM
44. Mates SP et al (2020) Dynamic Flow stress behavior of Hypo-Eutectoid Ferrite-Pearlite Steels under Rapid Heating. J Dynamic Behav Mater 6(2):246–265
45. Winchell P, Cohen M (1962) The strength of martensite. MASSACHUSETTS INST OF TECH CAMBRIDGE
46. Krauss G (1999) Martensite in steel: strength and structure. Mater Sci Engineering: A 273:40–57
47. Zhang F et al (2021) How austenitic is a martensitic steel produced by laser powder bed fusion? a cautionary tale. Metals 11(12):1924
48. Sathyanath A, Meena A (2020) Microstructural evolution and strain hardening behavior of heat-treated 17-4 PH stainless steel. Mater Today Commun 25:101416
49. Gladman T (1999) Precipitation hardening in metals. Mater Sci Technol 15(1):30–36
50. Hamada A et al (2013) Contribution of deformation mechanisms to strength and ductility in two Cr–Mn grade austenitic stainless steels. Mater Sci Engineering: A 559:336–344
51. Talonen J et al (2005) Effect of strain rate on the strain-induced $\gamma \rightarrow \alpha'$-martensite transformation and mechanical properties of austenitic stainless steels. Metall Mater Trans A 36(2):421–432
52. Robinson J, Shaw M (1994) Microstructural and mechanical influences on dynamic strain aging phenomena. Int Mater Rev 39(3):113–122
53. Guo Q et al (2022) Phase transformation dynamics guided alloy development for additive manufacturing. Additive Manuf 59:103068
54. Johnson GR (1983) A constitutive model and data for materials subjected to large strains, high strain rates, and high temperatures Proc. 7th Inf. Sympo. Ballistics, : p. 541–547
55. Habib SA, Meredith CS, Khan AS (2021) Quasi-static and dynamic investigation of an advanced high strength and corrosion resistant 10% Cr nanocomposite martensitic steel. Int J Mech Sci 211:106774
56. Robino C et al (1994) Heat treatment of investment cast PH 13 – 8 Mo stainless steel: part II. Isothermal aging kinetics. Metall Mater Trans A 25(4):697–704
57. Nelder JA, Mead R (1965) A simplex method for function minimization. Comput J 7(4):308–313
58. Virtanen P et al (2020) SciPy 1.0: fundamental algorithms for scientific computing in Python. Nat Methods 17(3):261–272
59. Vural M, Caro J (2009) Experimental analysis and constitutive modeling for the newly developed 2139-T8 alloy. Mater Sci Engineering: A 520(1–2):56–65